Journal of Sound and Vibration 640 (2026) 119886

Contents lists available at ScienceDirect

Journal of Sound and Vibration

journal homepage: www.elsevier.com/locate/jsvi

Direct and inverse approaches for modal detection using an external microphone array in the presence of a background flow

Michael Buba [a,b,*], Antonio Pereira [a], Christophe Bailly [a], Steffen Marburg [b], Marcus Maeder [b]

[a] Ecole Centrale de Lyon, CNRS, Universite Claude Bernard Lyon 1, INSA Lyon, LMFA, UMR5509, 69130, Écully, France
[b] Chair of Vibroacoustics of Vehicles and Machines, Technical University of Munich, Boltzmannstr. 15, 85748, Garching bei München, Bavaria, Germany

ARTICLE INFO

Keywords:
Modal detection
Far-field microphone array
Numerical simulation
Inverse method
Rotor-Stator interaction noise

ABSTRACT

Accurately characterizing the acoustic modal content generated by rotor-stator interaction in ducted fans is critical for noise mitigation. However, conventional in-duct measurement techniques are hampered by significant drawbacks, including limited physical space, intrusive sensor placement, and susceptibility to turbulent flow, all of which can compromise data accuracy.
In this paper, we introduce a methodology that determines the in-duct modal amplitudes from non-intrusive, external measurements. Our approach utilizes a hemispherical microphone array located in the far-field to capture the radiated acoustic pressure. This data, combining both experimental measurements and numerical simulations, is then processed using an iterative Bayesian Inverse Approach. This technique was specifically chosen to reconstruct the source modal content while effectively reducing the artifacts associated with array sidelobes. The results demonstrate that the modal amplitudes determined by our external measurements yield the same results as those from conventional in-duct approaches and even provide a higher degree of accuracy. This successful implementation, validated through a second test case with a modified outlet-guide-vane configuration, confirms that our method overcomes the core limitations of internal measurements. It offers a more robust and flexible approach for aeroacoustic analysis that is less sensitive to turbulent conditions and spatial constraints.

1. Introduction

One of the primary noise sources of a commercial aircraft is the engine. Innovations in the development of aircraft engines have led to a redesign to meet new regulatory requirements [1]. This includes shortening of the nacelle, larger fan diameters, and lower running fan speeds [2,3]. Engine manufacturers implemented these design changes, which led to the development of ultra-high bypass ratio (UHBR) engines.

The noise generated by turbofan engines can be broken down into tonal [4,5] and broadband noise [6]. Understanding the modal content inside the circular duct associated with the radiated tonal noise component is crucial for identifying appropriate countermeasures to reduce the noise emitted to the far-field. This comprises knowledge about the fan-outlet-guided-vane-generated noise, particularly the modal amplitudes of each propagating mode as a function of frequency. The reader can find a detailed recent review on the various methods to predict noise from rotor-stator interaction in Moreau & Roger [7]. The recent work by Al-Am et

* Corresponding author.
E-mail address: michael.buba@tum.de (M. Buba).

https://doi.org/10.1016/j.jsv.2026.119886
Received 27 October 2025; Received in revised form 8 May 2026; Accepted 11 May 2026
Available online 13 May 2026

Nomenclature

$A_{mn}^{\pm}$	complex-valued modal amplitudes
A_i^{in}	incident amplitude of the i-th acoustic mode
$\mathbf{B}$	total enthaply
B	number of rotor blades
$\mathbf{c}$	vector stacking complex-valued modal amplitudes A_{mn}
C	coefficients representing the geometrical boundary conditions
c_0	speed of sound
f_0	evaluation frequency
f_{mn}	normalized modal shape factor
$J_{\|m\|}$	m-th order solution of the Bessel's function of the first kind
j	imaginary unit
K	amount of microphones mounted on antenna
k_0	acoustic wavenumber
$k_{r_{mn}}$	radial wavenumber
$k_{z_{mn}}^{\pm}$	axial wavenumber
L	amount of propagating modes
M_z	Mach number
$\dot{m}$	mass flow rate
m	azimuthal mode order
n	radial mode order
$\mathbf{p}$	vector of Fourier coefficients of the acoustic pressure measured by in-duct microphones
$\tilde{\mathbf{p}}$	vector of Fourier coefficients of the acoustic pressure measured by external microphones
$p_e(\mathbf{r}_i)$	experimentally measured acoustic pressure at position $\mathbf{r}_i$
$\mathbf{r}$	position vector
$\mathbf{r}_i$	discrete location of the i-*th* microphone
r_d	duct radius
S	surface of the duct's cross section
$\mathbf{S_{cc}}$	cross-spectral matrix of mode coefficients
$\mathbf{S_{pp}}$	cross-spectral matrix of measurements
T	temperature
$\mathbf{u}_0$	background mean flow velocity
V	number of stator vanes
$W_{m,n}$	sound power level of a given mode of azimuthal order m and radial order n
Z_0	specific acoustic impedance
z	axial coordinate
β	Prandtl-Glauert factor
Γ_{mn}	Mode normalization factor
κ_{mn}	zero value of the first derivative of the Bessel's function of first kind
$\mathbf{\Phi}$	transfer matrix
ϕ	acoustic velocity potential
φ	phase shift along the duct's axis
Ω	angular frequency
$\boldsymbol{\omega}$	vorticity
θ	polar angle
ρ	density
$\tilde{(\cdot)}$	quantity associated with the external microphone array
$\hat{(\cdot)}$	quantity associated with the external microphone array assuming background mean flow velocity fluctuation
$\bar{(\cdot)}$	quantity associated with the external microphone array assuming array positioning misplacement
$\breve{(\cdot)}$	quantity associated with the external microphone array assuming different normalization parameters for iBIA
$\dot{(\cdot)}$	time derivative
$(\cdot)'$	fluctuating parameter
$(\cdot)^{\dagger}$	reconstructed quantity through a inverse operation
$(\cdot)^{-}$	upstream propagation
$(\cdot)^{+}$	downstream propagation
$(\cdot)_0$	ambient values

al. [8–10] may be mentioned in particular, based on high-fidelity numerical simulation. The broadband noise radiated by an ultra-high bypass ratio fan/outlet-guide-vane (OGV) configuration is directly calculated using compressible large eddy simulation for a

full annulus geometry. Many details of the complex turbulent flow and its acoustics are revealed with this spectacular computational effort, for the fan wake-OGV interaction [8,9] as well as for the noise induced by the clearance between the fan tip and the curved wall [10]. Numerical simulations of sound radiation from a circular duct, including directivity calculations, are becoming increasingly important and are increasingly being considered numerically [11].

Early investigations in this field of research dealing with the measurement of spinning acoustic modes were conducted by Mugridge [12] during the 1960s. Using a space and time correlation technique of two transducers' signals, the type of acoustic mode and its contribution to the total tone signal can be determined by hot-wire anemometers [12]. The introduction of microphones simplifies the data acquisition and therefore the determination of the azimuthal and axial wavenumber spectra, as well as of the modal structure of the sound field for a given frequency [13]. While Harel et al. [13] determine the modal content by means of various signal correlation methods and the Fast-Fourier Transformation (FFT), Pickett et al. [14] develop an in-duct modal decomposition technique, where the positions of the microphones are determined using a special procedure to avoid numerical instability. The modal amplitudes are hereby determined by solving a linear system of equations using matrix inversion. Over time, researchers have increasingly focused on investigating higher-order acoustical modes across a wide frequency range by introducing microphones along the duct's axis, both circumferentially and radially. Using more than two traversing microphones allows Moore [15] and Enghardt [16] to identify azimuthal and radial duct modes. A more advanced method consists of determining the circumferential and radial modes using rotating microphone rakes [17–20]. However, the latter approaches are limited by the need for a large number of array positions and multiple fixed reference probes. Alternatively, one can use many fixed, wall-mounted microphones distributed along the duct. In order to circumvent this issue, Joppa [21,22] introduces a new approach that employs circumferential and axial microphone arrays to determine the sound level as a function of the spinning order using spatial Fourier transformation in order to design effective linings for noise reduction purposes. Sarin et al. [23] makes use of this method and develops it further in order to examine the circumferential modal amplitudes during in-flight tests by circumferential microphone rings, while Rademaker et al. [24] introduce a sparse microphone array instead of an equidistant one.

However, the use of internal microphone arrays comes with some disadvantages that should not be overlooked. Radial traverse microphone support structures generate flow-induced noise, as well as distortion of the background flow. The generated turbulence has an impact on the rotor blades, producing additional broadband noise. Another aspect is the low signal-to-noise ratio of the measurements due to wall-flush mounted microphones that are submitted to turbulent boundary layer noise. For the mentioned reasons, Lowrie and Tester first utilize far-field measurements to predict the modal content generated by a ducted fan stage [25,26]. Far-field measurements are more beneficial as the microphone probes are not disturbed by turbulent flow noise. Moreover, a far-field microphone array can be used to test different engine types without the need to mount and unmount the microphones, which entails a lower workload and time savings. Far-field microphone arrays can be used in anechoic chambers, where wall reflections do not appear, and the measurement data is therefore more reliable. By identifying the far-field patterns, it is possible to determine the modal content of the sound field using the so-called Polar Correlation Technique [25–27]. Another technique discussed in the literature is the use of a circular hoop microphone array centered on the duct axis [28–30]. Sound pressure is measured at several axial positions, where it is decomposed into azimuthal modes. A Rayleigh integral is then used to model the radiation from the inlet, establishing a relationship between azimuthal and radial mode amplitudes. One drawback of this approach is that measurements are performed sequentially, requiring the reconstruction of phase relationships between successive positions. This is relatively easy for tonal noise components but more challenging for broadband components.

The estimation method constitutes another major component in mode detection problems, as determining of the modal content using in-duct measurements comes with some limitations. Early methods employ simple calculation algorithms, such as spatial Fourier transforms, to estimate the modal content. Fundamental research in the field of inverse calculation techniques for determining the strengths of acoustic noise sources has been carried out by Nelson et al. [31,32] and particularly by Kim et al. [33], who employs singular value decomposition in the case of circular ducts. Lewy [34] further develops the inverse problem approach to detect the modal structure of an acoustic field consisting of spinning modes caused by a ducted turbofan stage using conventional far-field directivity measurements. One of the main findings for using the pseudo-inverse calculation approach is the necessity to ensure that the number of pressure probes measuring the acoustical pressure is higher than the number of propagating modes [35]. For high-frequency applications or when the number of microphones is smaller than the number of propagating modes, sophisticated numerical methods for solving the inverse problem must be used, as high condition numbers may result. This problem can be bypassed through regularization techniques. Castres et al. [36–38] propose a technique to detect modal amplitudes within broadband fan noise using near-field microphone arrays. They first introduce inverse calculation methods to determine the modal amplitudes of both the azimuthal and radial duct acoustic modes by relating the numerically calculated and measured pressure data. More recently, Etchebarne et al. [39] use an external planar array to reconstruct the in-duct modal amplitudes in a simplified geometry without background mean flow. Thereby, a deconvolution approach is used to estimate the modal amplitudes. A comparison of mode amplitudes estimated by an in-duct array has shown some discrepancies between exterior and interior measurements.

In the present study, an experimental approach is considered to estimate the modal content of a fan-OGV stage by extending the previous pioneering work of Castres & Joseph [36,37]. The radiated acoustic field is measured using an external hemispherical microphone array, and an inverse method is employed to determine the modal amplitude of the acoustic field within the duct. This initial approach does not take background mean flows into account as the radiated sound pressure is modeled using directivity patterns based on the Kirchhoff approximation for flanged ducts. One of the novelties in the present work is the consideration of a background mean flow induced by the fan. Each mode's transfer function is determined numerically by solving the wave equation in the presence of a background potential flow. A realistic intake geometry, including background mean flow effects, is considered. All the measurements are performed in a well-documented test bench denoted as LP3 [40,41]. The motivation for developing this approach is to identify

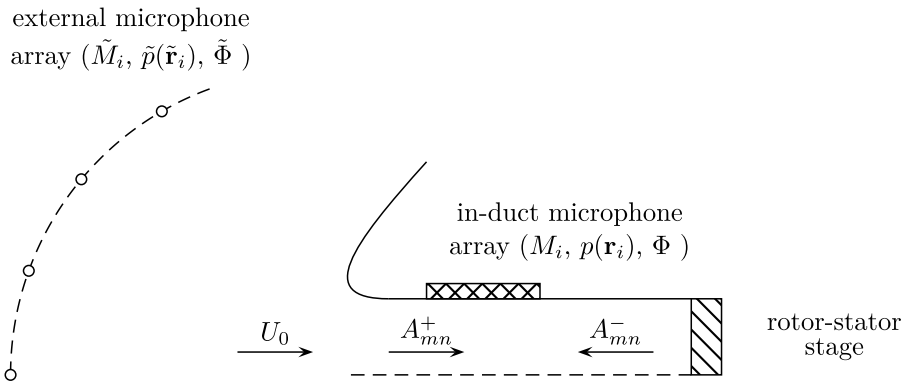

Fig. 1. Schematic representation of the problem. Upstream-propagating modes A^-_{mn} are generated by a sound source (e.g., a rotor-stator stage), which also induces an axial mean flow with velocity U_0. Due to impedance mismatch at the duct inlet, part of the acoustic energy is reflected, generating downstream-propagating modes A^+_{mn}. An internal microphone array composed of M_i microphones measures the acoustic pressure $p(\mathbf{r}_i)$ at discrete locations $\mathbf{r}_i$ inside the duct. A second array of $\tilde{M}_i$ microphones is positioned on a hemispherical surface surrounding the duct inlet, recording the acoustic pressure $\tilde{p}(\tilde{\mathbf{r}}_i)$ at positions $\tilde{\mathbf{r}}_i$.

the internal acoustic modal content in the nacelle without the need for an internal microphone antenna, as recent developments in aircraft engine design are leading to shorter nacelles, resulting in less space available for measuring instruments. Due to a shorter axial extent, the distance between the pressure probes is smaller and, hence, the identification of radial modes becomes more difficult as some modal axial wavelengths may be larger than the axial extent of the microphone array. Using external microphones is therefore a good compromise as we can better discretize these modes. The inverse approach's estimate is compared to the direct approach's result, which is measured using the internal microphone array. The transfer function between duct modes and external microphones is computed by a direct approach using numerical simulation software. The modal amplitudes are estimated by an advanced inverse technique previously described by Pereira and Jacob [42]. The remainder of this paper is organized as follows. Section 2 gives an overview of the problem statement and provides a novel solution approach. Section 3 describes the theoretical framework underlying the modal decomposition methodology and discusses briefly the mode detection approach. Section 4 presents the simulation approach by discussing the underlying equations implemented in the numerical software. Section 5 describes the experimental test setup and the measurement campaign for determining modal content prior to the summary of this work and comments on the newly developed methodology presented in Section 6.

2. Problem formulation, methodology and objective

The problem addressed in this study involves a sound source, in this case a rotor-stator stage, radiating acoustic waves into a duct including a background mean flow, presented in Fig. 1. In this work, only the forward arc noise is investigated, and therefore, only upstream-propagating modes generated by the source are considered. Downstream-propagating modes arise solely from reflection at the duct's open end due to impedance mismatch at the inlet. It is assumed that these reflected waves are not reflected upstream upon reaching the rotor blades, thus preventing the formation of stationary longitudinal waves between the open end and the rotor-stator stage. An in-duct microphone array decomposes the acoustic field into duct modes. Using analytical formulations, the acoustic pressure field can be expressed in terms of upstream-propagating modes (A^-_{mn}) and downstream-propagating modes (A^+_{mn}). The presented approach replaces the current analytical propagation models with a numerical simulation model that considers the reflection and transmission at the open end. This allows the identification of only the upstream modes (A^-_{mn}), which reduces the number of unknowns by one half. Moreover, the numerical model provides a transfer function between these incident modes and the acoustic pressure at the measurement points located on a hemisphere surrounding the duct. The numerical simulation incorporates both the background mean flow and the precise geometry of the intake lip. Quantities associated with the measurements of the external microphone antenna are depicted by a tilde ($\tilde{\cdot}$), while quantities representing in-duct measurements are displayed without any special characters.

To compute the transfer function, a direct problem is solved by injecting incident modes with unitary amplitude ($A^-_{mn} = 1$) independently, and simulating the resulting propagation to both in-duct $p(\mathbf{r}_i)$ and far-field microphones $\tilde{p}(\tilde{\mathbf{r}}_i)$, see Eq. (1).

$$\begin{aligned} \tilde{p}(\tilde{\mathbf{r}}_i) &= \tilde{\Phi}_{mn} A^-_{mn} \quad \text{with} \quad A^-_{mn} = 1 \quad \forall_{m,n} \quad \text{cut-on}\,, \\ p(\mathbf{r}_i) &= \Phi_{mn} A^-_{mn} \quad \text{with} \quad A^-_{mn} = 1 \quad \forall_{m,n} \quad \text{cut-on}\,. \end{aligned} \tag{1}$$

The resulting transfer functions $\tilde{\Phi}_{mn}$ and Φ_{mn} relate each incident mode to acoustic pressure at the respective microphone locations. These functions are then combined with experimental microphone data $\tilde{p}_e(\tilde{\mathbf{r}}_i)$ and $p_e(\mathbf{r}_i)$ to formulate two inverse problems, one based on far-field data and the other one on in-duct measurements, see Eq. (2). Solving these inverse problems yields the estimated mode

amplitudes generated by the source.

$$\begin{aligned} \tilde{A}^{-}_{mn} &= \mathcal{F}^{-1}\left(\tilde{\Phi}_{mn}\right)\tilde{p}_e(\tilde{\mathbf{r}}_i)\,, \\ A^{-}_{mn} &= \mathcal{F}^{-1}\left(\Phi_{mn}\right)p_e(\mathbf{r}_i)\,. \end{aligned} \tag{2}$$

The objective of this paper is to determine the experimental incident mode amplitudes that best reconstruct the measured acoustic fields. Emphasis is placed on how the numerical model is used to compute the transfer functions, and a comparison is presented between mode detection based on in-duct versus far-field measurements using experimental data.

3. Theoretical background

This section summarizes the theoretical background that describes the in-duct sound pressure field and outlines the modal detection calculation approach.

3.1. Modal description of the acoustic pressure field inside a duct

The complex acoustic pressure $p(z, r, \theta)$ of a stationary sound field inside a hard-walled duct with circular cross-section can be expressed by a weighted sum of modes

$$p(z, r, \theta) = \sum_{m=-\infty}^{\infty}\sum_{n=0}^{\infty}\left[A^{+}_{mn}\mathrm{e}^{\mathrm{j}k^{+}_{z_{mn}}z} + A^{-}_{mn}\mathrm{e}^{\mathrm{j}k^{-}_{z_{mn}}z}\right]f_{mn}(r)\,\mathrm{e}^{\mathrm{j}m\theta}\,. \tag{3}$$

where A^{+}_{mn} and A^{-}_{mn} are the complex-valued amplitudes depending on the azimuthal and radial mode orders m and n [43]. Note that in the framework of this work, an $\mathrm{e}^{-\mathrm{j}\Omega t}$ time-harmonic convention is used. The axial wavenumbers are denoted by $k^{\pm}_{z_{mn}}$ according to the azimuthal and radial mode orders, as well as the upstream ($^{-}$) and downstream ($^{+}$) propagation direction of the acoustic wave. The normalized modal shape factor $f_{mn}(r)$ depends on the duct's cross-section and is for a circular duct

$$f_{mn}(r) = \frac{J_{|m|}(k_{r_{mn}}r)}{\Gamma_{mn}}, \tag{4}$$

where $J_{|m|}$ is the m-th order Bessel function of the first type and Γ_{mn} is a normalization factor according to Pereira and Jacob [42]. The axial wavenumber $k^{\pm}_{z_{mn}}$ reads

$$k^{\pm}_{z_{mn}} = \frac{1}{\beta^2}\left(-M_z k_0 \pm \hat{k}_{r_{mn}}\right), \tag{5}$$

and depends on the Mach number $M_z = U_0/c_0$ along the axial direction z and the squared Prandtl-Glauert factor $\beta^2 = 1 - M_z^2$. The acoustic wave number $k_0 = \Omega/c_0$ consists of c_0 that represents the speed of sound, U_0 the velocity of the background mean flow, and Ω the angular frequency. The $\hat{k}_{r_{m,n}}$ term is a modified radial wavenumber defined as

$$\hat{k}_{r_{mn}} = \sqrt{k_0^2 - \beta^2 k^2_{r_{mn}}}, \tag{6}$$

which depends on the radial wavenumber

$$k_{r_{mn}} = \frac{\kappa_{mn}}{r_d}, \tag{7}$$

where r_d is the duct radius and κ_{mn} the n-th root of the first derivative of the Bessel's function J_m of order m. The modified radial wavenumber $\hat{k}_{r_{mn}}$ plays a key role as it determines whether an acoustic mode becomes propagating, a so-called cut-on mode. The number of cut-on modes propagating through a circular duct depends mainly on the duct's radius r_d, the considered angular frequency Ω, and the background mean flow velocity. Rienstra *et al.* provide more detailed information on the theoretical foundations of acoustic mode propagation in circular ducts [44].

3.2. Mode detection problem

The acoustic pressure field is sampled by either in-duct microphones M_i or external microphones $\tilde{M}_i$. The unknown mode amplitudes A_{mn} are related to microphone data using either an analytical or a numerical propagation model. Only cut-on modes are considered in the model, as the microphones are placed far from the source. The infinite series in Eq. (3) is truncated up to an azimuthal order m and radial order n of cut-on modes. According to Fig. 1 the acoustic pressure $p(\mathbf{r}_i)$ is measured at $\mathbf{r}_i$ positions in the duct. For a given frequency f_0, these measurements can be arranged into a column vector $\mathbf{p} \in \mathbb{C}^K$ after applying a Fourier transform. Eq. (3) can then be written as a matrix-vector product as

$$\mathbf{p} = \mathbf{\Phi}\mathbf{c}, \tag{8}$$

where $\mathbf{c} \in \mathbb{C}^L$ contains the complex-valued amplitudes A^{-}_{mn} of all L cut-on modes in terms of the mode orders (m, n). The matrix $\mathbf{\Phi} \in \mathbb{C}^{K\times L}$ represents the transfer function that incorporates the propagation model. Mode detection aims to solve Eq. (8) for the unknown variable $\mathbf{c}$, by which the modal amplitudes of the propagating modes are estimated. Assuming stationarity and ergodicity of the measured signals over time, one can rewrite Eq. (8) in terms of the cross-spectral matrix of measurements $\mathbf{S}_{\mathbf{pp}}$. This

cross-spectral density matrix is defined as $\mathbf{S_{pp}} \triangleq \mathbb{E}\{\mathbf{p}\mathbf{p}^H\}$ including the Hermitian vector $\cdot^H$ and the expected value $\mathbb{E}\{\cdot\}$. Eq. (8) then becomes

$$\mathbf{S_{pp}} = \mathbf{\Phi}\mathbf{S_{cc}}\mathbf{\Phi}^H, \tag{9}$$

where $\mathbf{S_{cc}} \triangleq \mathbb{E}\{\mathbf{c}\mathbf{c}^H\}$ is the cross-spectral matrix of mode coefficients. The goal of the inverse problem is to solve Eq. (9) for $\mathbf{S_{cc}}$. Different approaches have been proposed to address the mode detection problem, including least-squares beamforming [45,46], deconvolution techniques [47,48], regularized ℓ_2-norm inverse methods [36,40], and minimization under sparsity constraints [49–51]. This work employs an iterative Bayesian Inverse Approach (iBIA). The approach and the implemented algorithm have been described in a previous study [42]. It has been shown that iBIA, when combined with a sparsity-enforcing prior and irregular microphone array configurations, improves the dynamic range by reducing artifacts caused by mode aliasing. Since the regularization procedure in iBIA is fully automated, the only parameter that needs to be set by the user is the ℓ_p-norm used in the minimization problem. In this work, the analysis focuses on the tonal noise components associated with the rotor-wake-stator interaction. Consequently, the modal content is expected to be sparse since according to the Tyler and Sofrin's rule [4] only a few specific modes are favored. Therefore, the parameter p is set to 1, and the ℓ_1-norm is employed. This choice provides a good compromise between the ℓ_0-norm, which enforces strong sparsity but is more difficult to solve and the ℓ_2-norm that leads to a classical inverse problem with Tikhonov regularization [42]. It should be emphasized that the *a priori* sparsity assumption applies to the solution coefficient vector $\mathbf{c}$ rather than to the modal basis $\mathbf{\Phi}$ (i.e., the transfer function). According to the Tyler and Sofrin's rule, rotor-stator wake-interaction at the blade passing frequencies generate only the discrete set of azimuthal modes satisfying $m = kB - sV$, where m is the azimuthal order, k the harmonic index of the blade passing frequency (BPF), B the number of rotor blades, V the number of stator vanes, and s an integer. The range of cut-on modes is determined by the rotor rotational speed, duct diameter, and axial Mach number. In the present case, the number of propagating modes generated by the wake-interaction noise is small compared with the total number of cut-on modes in the modal basis, which supports the sparsity assumption on the coefficient vector $\mathbf{c}$. Once the mode amplitudes are estimated, the acoustic power $W_{m,n}$ carried by each mode can be computed through

$$W_{mn}^{\pm} = \frac{k_0 S \beta^4}{2Z_0} \frac{\sqrt{k_0^2 - \beta^2 k_{r_{mn}}^2}}{\left(k \mp M_z \sqrt{k_0^2 - \beta^2 k_{r_{mn}}^2}\right)^2} |A_{mn}^{\pm}|^2, \tag{10}$$

where $S = \pi r_d^2$ the duct's cross-section surface and $Z_0 = \rho_0 c_0$ the specific acoustic impedance [42]. The total transmitted sound power results by summation of Eq. (10) over all cut-on azimuthal mode orders M and radial mode orders N as:

$$W_{\text{tot}}^{\pm} = \sum_{m=-M}^{m=M} \sum_{n=0}^{n=N} = \frac{k_0 S \beta^4}{2Z_0} \sum_{m=-M}^{m=M} \sum_{n=0}^{n=N} \frac{\sqrt{k_0^2 - \beta^2 k_{r_{mn}}^2}}{\left(k \mp M_z \sqrt{k_0^2 - \beta^2 k_{r_{mn}}^2}\right)^2} |A_{mn}^{\pm}|^2. \tag{11}$$

In the next section, the numerical approach to compute the modal basis (i.e., transfer function) related to the in-duct microphone array $\mathbf{\Phi}$ and to the external microphone array $\tilde{\mathbf{\Phi}}$ is described.

4. Numerical simulation approach

The propagation of higher-order ducted modes to the far-field, considering a background mean flow, is modeled numerically using a finite element solver. Existing analytical methods are limited to simplified geometries, such as infinitely thin circular ducts [52,53] or annular ducts [53], and ducts mounted on an infinite baffle. When background mean flow is considered, only the case of a duct immersed in a uniform mean flow has typically been considered. This differs from static test conditions, where the surrounding flow is at rest and accelerates as it is drawn into the duct. In this work, the propagation of higher-order duct modes to the far-field, accounting for both the exact intake lip geometry and the background mean flow, is modeled numerically using the commercial software COMSOL MULTIPHYSICS. The computation yields the matrix of transfer functions between duct modes and either in-duct microphones $\mathbf{\Phi}$ or far-field microphones $\tilde{\mathbf{\Phi}}$.

4.1. Theoretical background of the numerical method

Prior to the propagation of acoustic waves, a numerical simulation of the background mean flow has to be performed. The compressible potential flow theory is used to determine the background mean flow $\mathbf{u}_0$. As only the background mean flow's influence on acoustic modes' propagation is investigated in this study, and turbulence is disregarded here. The compressible potential flow theory assumes an ideal, homentropic fluid flow with zero viscosity and no thermal conduction [54–56]. After calculating the background flow using the compressible potential flow equations, these are linearized and divided into a background component ϕ_0 related to the steady base flow and the acoustic fluctuating field component ϕ' represented by

$$\phi = \phi_0 + \phi' . \tag{12}$$

The governing equation describing the propagation of acoustic modes in the presence of a background mean flow is solved numerically by COMSOL MULTIPHYSICS is denoted as:

$$-\frac{\rho_0}{c_0^2}\frac{\partial}{\partial t}\left(\frac{\partial \phi'}{\partial t} + \mathbf{u}_0 \cdot \nabla \phi'\right) + \nabla \cdot \left[\rho_0 \nabla \phi' - \frac{\rho_0}{c_0^2}\left(\frac{\partial \phi'}{\partial t} + \mathbf{u}_0 \cdot \nabla \phi'\right)\mathbf{u}_0\right] = 0 . \tag{13}$$

Eq. 13 is based on the vortex sound equation according to Howe [56] and incorporates a compressible potential flow that acts as the background mean flow. The derivation of this equation is discussed in more detail in the Appendix A.

The acoustic velocity potential is first computed over a two-dimensional domain and then revolved around the central axis to obtain an axisymmetric three-dimensional geometry that is described by the following relation:

$$\phi = \phi(\mathbf{r})\, e^{\mathrm{j}k_{z_{mn}} z - \mathrm{j}m\theta}. \tag{14}$$

The axial wavenumber $k_{z_{mn}}$ and shape of the velocity potential ϕ' are calculated internally within a second simulation step by the simulation software. These are used to determine the propagation of acoustic modes from the boundary surface through the circular duct into the far-field domain. The simulation software internally computes the spatial distribution of the velocity potential ϕ', as well as the axial wavenumber $k_{z_{mn}}$, that are used to characterize the propagation of acoustic modes from the lower boundary surface through the circular duct into the far-field domain. The pre-implemented 'port'-condition [57] acts as a sound source by exciting and absorbing specific acoustic modes on a given boundary. This boundary condition emits single acoustic modes with uniform amplitudes A_{mn} in the upstream direction and absorbs all reflected downstream propagating modes as a perfectly matched layer. This port condition is used to construct the transfer functions $\tilde{\Phi}_{mn}$ and Φ_{mn} by emitting single modes that do not interact with other modes.

4.2. Implementation of the model

The aeroacoustics branch of COMSOL MULTIPHYSICS is used, as it combines the background mean flow and acoustic simulation through multiphysics coupling. The numerical simulations are performed using COMSOL MULTIPHYSICS to model acoustic modes, including higher azimuthal and radial orders than in plane-wave propagation, in the presence of a background mean flow. The accuracy of the simulation software has been demonstrated in a previous study by comparing the directivity patterns of acoustic modes as they exit a circular duct [11]. The numerical simulation results closely match the directivity pattern calculated using an analytical solution for ducted-mode propagation, as discussed by Ford et al. [41]. In this work, comparison with analytical results confirms that transfer functions derived from COMSOL MULTIPHYSICS simulations are sufficiently accurate and reliable for predicting mode-dependent sound radiation in ducts. A visualization of the geometry is depicted in Fig. 2a. The circular duct is modeled using a two-dimensional axisymmetric domain, which is particularly beneficial in terms of computational effort and storage capacity compared to three-dimensional geometries. A spherical far-field domain is surrounded by a perfectly matched layer (PML) domain, which ensures that acoustic waves are not reflected at the edge of the model boundary and radiated back into the calculation field, distorting the results. The duct's lower end is initialized by the 'port'-condition and the corresponding velocity potential ϕ, whereupon specific acoustic modes are propagated into the computational domain. The entire boundary, which is not located on the symmetry axis, is considered sound-reflecting. The solid line, located 0.7 m from the inlet, represents the position of the semi-spherical, three-dimensional microphone array. The values of ambient pressure, density, and temperature of air are $p_0 = 99\,181$ Pa, $\rho_0 = 1.149\,\mathrm{kg/m^3}$ and $T_0 = 300.7\,^\circ$K, respectively, according to the experimental conditions. The considered domain is discretized by a triangular mesh for both the background mean flow and the acoustic simulation. The background mean flow is calculated as compressible potential flow without vorticity. This simulation utilizes a single mesh optimized for acoustic properties, thereby avoiding complex transformations between various mesh types and saving computational effort and time. A triangular mesh is used within the two-dimensional geometry with a minimum and maximum size of 1 mm and 5 mm. Since the three critical blade-passing frequencies are in the range

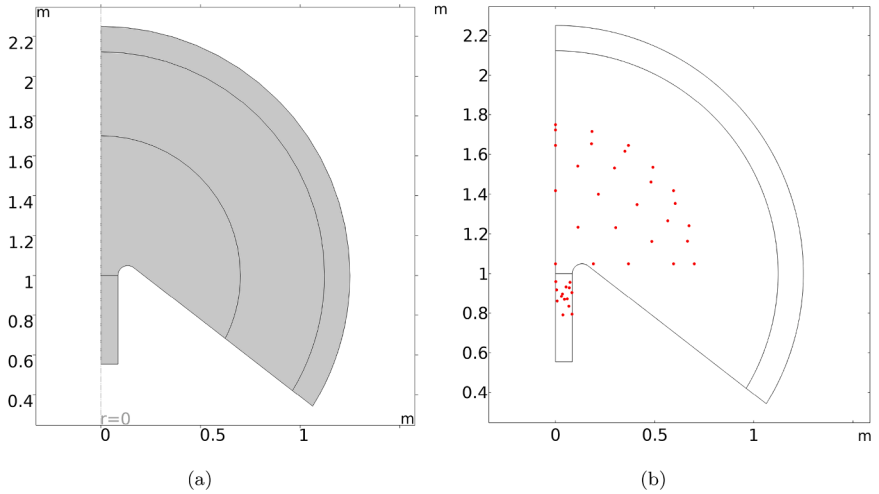

Fig. 2. (a) Visualization of the geometry implemented in COMSOL MULTIPHYSICS. The duct is located at the bottom of the domain, from where the acoustic modes are radiated into the far-field via the bellmouth-shaped inlet. (b) Visualization of the microphone array coordinates in the numerical simulation. This two-dimensional figure illustrates the locations of both microphone arrays: the external far-field array, located outside the duct, and the in-duct microphone array.

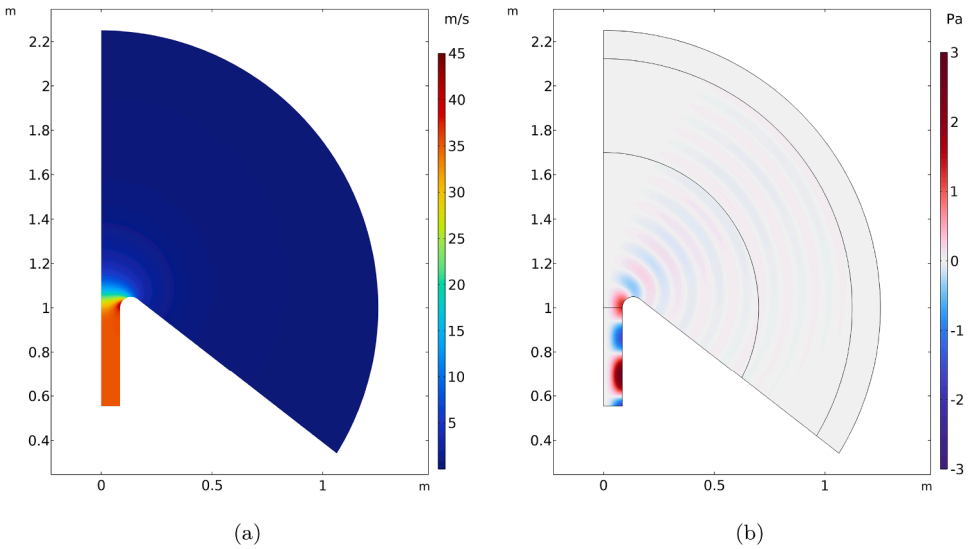

Fig. 3. (a) Visualization of the velocity of the background mean flow and (b) of the arbitrarily chosen acoustic mode $(3,0)$ propagating into the far-field domain towards the spherical microphone array.

below 10 000 Hz, a maximum mesh size of 5.7 mm should be used, taking into account the requirement that six mesh elements fit within one wavelength to ensure accuracy. Lagrangian shape functions of quadratic order discretize the system. In total, the simulation consists of 149982 elements. Fig. 2b depicts the location of the measurement points within the numerical simulation. They are placed in identical positions around the intake of the circular duct and within the duct, as in the experimental setup.

4.3. Simulation approach

The numerical simulation is divided into three separate simulation steps. In the first simulation step, the background mean flow is calculated by means of the potential flow theory described in Section 4.1. A mass flow rate of $\dot{m} = 1\,\mathrm{kg\,s^{-1}}$ enters the duct from the far-field domain and propagates through the duct toward the fan stage position. The numerical simulation determines the background mean flow velocity $\mathbf{u}_0$, which is used for further calculations of mode propagation. In a second simulation step, all propagating modes depending on the mode order (m,n) are calculated. The so-called 'boundary mode' analysis determines the axial wavenumber $k_{z_{mn}}$ as well as the mode shape of the velocity potential Φ'^{-} for all upstream and Φ'^{+} downstream propagating modes. The third simulation step propagates the acoustic modes into the far-field domain based on the prior calculated axial wavenumber and acoustic velocity potential by using Eq. 13. The results of the first and third simulation steps are displayed in Fig. 3. Fig. 3a visualizes the flow velocity in the far-field and within the circular duct by assuming the compressible potential flow theory. This indicates that the velocity of the background mean flow in the far-field is approximately $0\,\mathrm{m\,s^{-1}}$, increases near the inlet, and ultimately reaches a speed of $\mathbf{u}_0 = 35.42\,\mathrm{m\,s^{-1}}$ within the duct. Fig. 3b shows an example of the propagation of acoustic mode $(3,0)$ at the first Blade Passing Frequency (BPF). The outermost layer delineates the PML layer, whereas the solid line in the far-field domain, positioned 0.7 m downstream of the inlet, represents the location of the spherical microphone array.

In the following, the radiation of duct modes into the far field is examined in more detail. Fig. 4 illustrates the propagation of acoustic waves from the lower boundary of the duct, corresponding to the location of the fan-OGV stage, into the far field. Each subfigure superimposes the acoustic wave field with the positions of the microphones mounted on the external array and inside the duct, depicted as small black dots. A cross-sectional view in the vicinity of the fan-OGV stage is additionally shown to the right of the duct in each subfigure. For visualization purposes, the three-dimensional microphone positions are projected onto a two-dimensional plane.

Fig. 4 shows the real part of the simulated acoustic pressure for several modes at the second BPF ($k_0 r_d = 8.8$). Results are presented for azimuthal orders m ranging from -1 to 1 and radial orders n from 0 to 2. In the adopted notation, the (0,0) mode corresponds to the plane wave. Owing to the 2D representation, positive and negative azimuthal orders exhibit identical pressure patterns, however, they rotate in opposite directions as they propagate along and outside the duct. Each mode produces a distinctive radiation pattern as it exits the duct. For higher radial orders ($n > 0$), the radial pressure structure, particularly the presence of pressure nodes, translates into directivity dips as the wave propagates into the far field, resulting in characteristic radiation patterns. Modes close to their cut-off frequency, such as $(-1,2)$ and $(1,2)$, exhibit a larger axial wavelength (see Fig. 4(g) and Fig. 4(i)). For these modes, a stronger difference between the pressure amplitude inside the duct and the external acoustic field is also observed. This behavior is consistent with the well-known increase in the modal reflection coefficient at the open duct termination as the cut-off condition is approached.

Results are also shown for higher azimuthal orders at the third BPF ($k_0 r_d = 13.2$), see Fig. 5. As the azimuthal order increases, the modal energy becomes increasingly concentrated near the duct wall. Consequently, the far-field radiation shifts toward larger

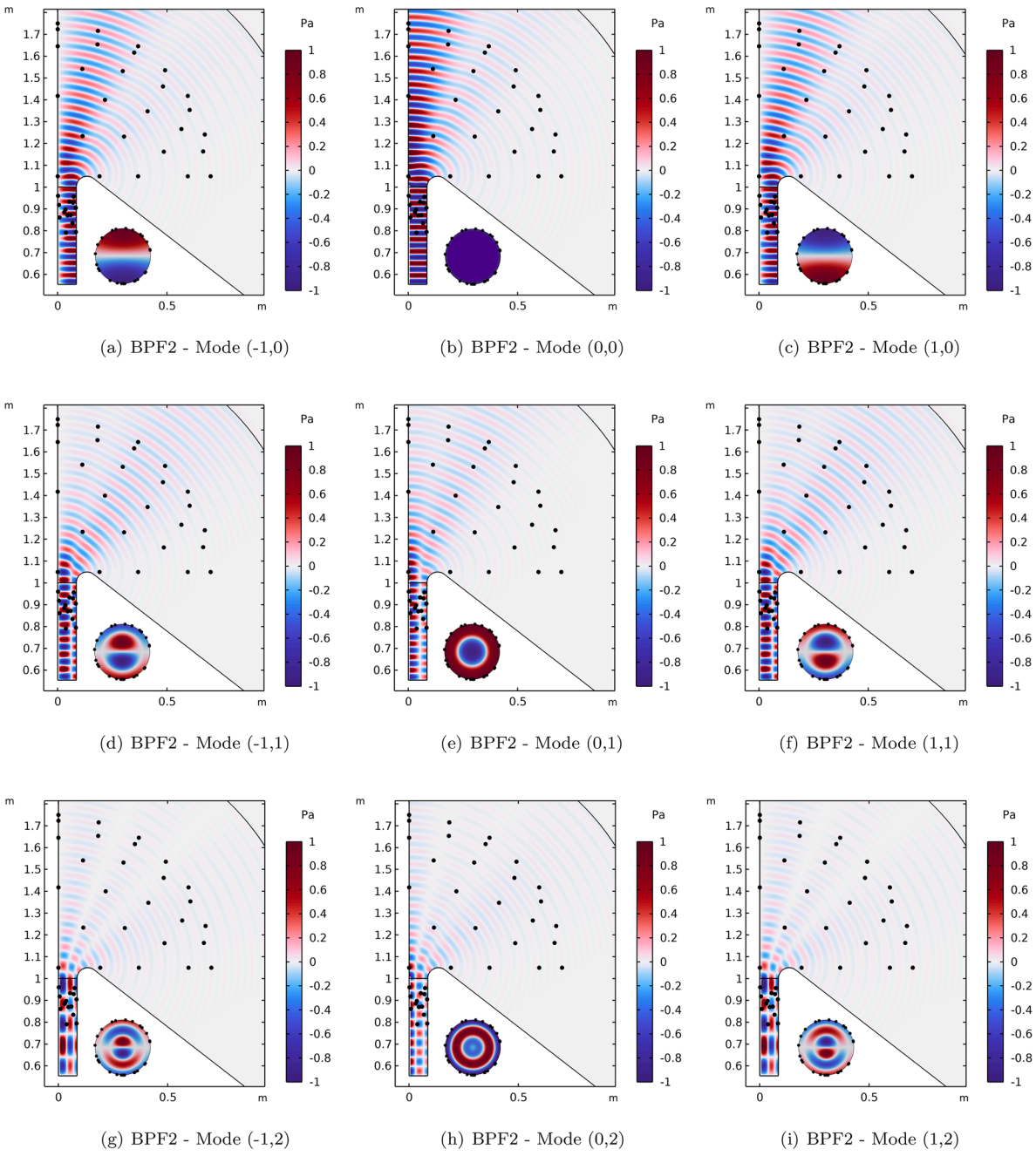

(a) BPF2 - Mode (-1,0) (b) BPF2 - Mode (0,0) (c) BPF2 - Mode (1,0)

(d) BPF2 - Mode (-1,1) (e) BPF2 - Mode (0,1) (f) BPF2 - Mode (1,1)

(g) BPF2 - Mode (-1,2) (h) BPF2 - Mode (0,2) (i) BPF2 - Mode (1,2)

Fig. 4. 2D representation of the real part of the acoustic pressure field obtained with the finite element solver for different azimuthal and radial modes (m,n) at the second BPF. Black dots indicate the positions of the in-duct and external microphone arrays. A cross-sectional view of the pressure field inside the duct is included to highlight the azimuthal variation of the pressure pattern. This view with projected microphone positions is magnified for visualization purposes.

directivity angles relative to the duct axis. This representation provides useful physical insight for interpreting the microphone array performance metrics, namely the condition number and the mutual coherence, to be presented in Section 5.3.

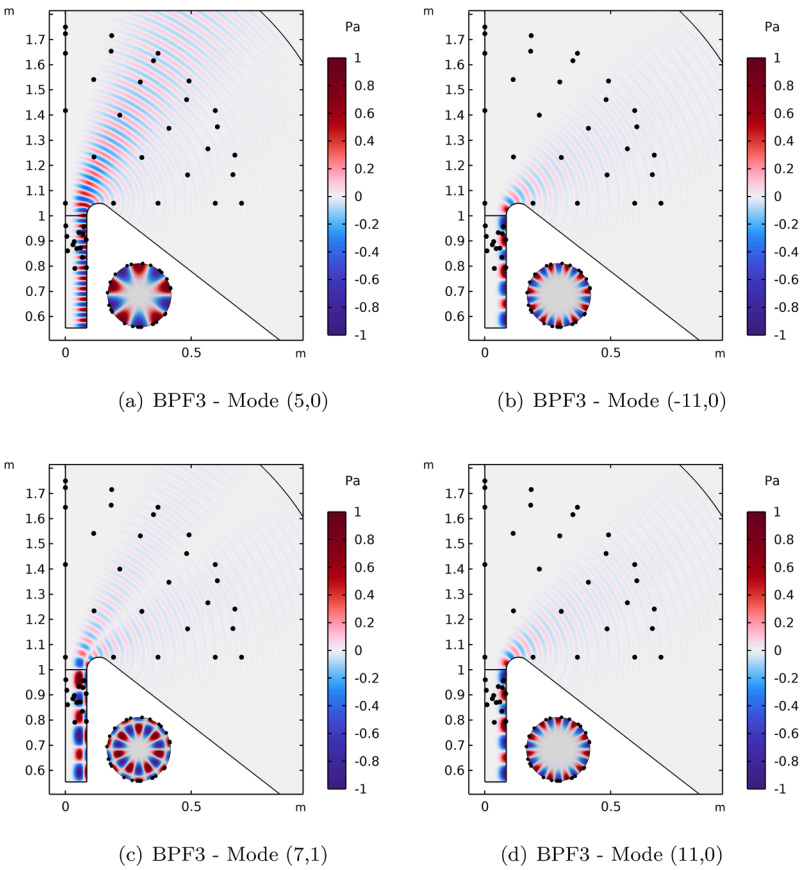

(a) BPF3 - Mode (5,0)

(b) BPF3 - Mode (-11,0)

(c) BPF3 - Mode (7,1)

(d) BPF3 - Mode (11,0)

Fig. 5. 2D representation of the real part of the acoustic pressure field obtained with the finite element solver for a few different modes at the BPF3. Black dots indicate the positions of the in-duct and external microphone arrays. A cross-sectional view of the pressure field inside the duct is included to highlight the azimuthal variation of the pressure pattern. This view with projected microphone positions is magnified for visualization purposes.

5. Experimental validation

5.1. The LP3 test bench

The numerically computed transfer functions from the previous section are tested using experimental data. The data are measured in a low-speed axial-flow test bench located at École Centrale de Lyon in France. Fig. 6 presents an overview of the test bench.

A Turbulence Control Screen (TCS) is used to suppress inlet flow distortions. Static pressure and total temperature probes are employed to control the operating point by measuring the stage's pressure rise and the mass flow rate via a Venturi tube. A gate valve, located downstream of an anechoic plenum, is used to adjust the operating point. The airflow is ejected into the same room, and an anechoic duct termination is used to prevent exhaust noise from polluting external measurements. The source under study is a low-speed electrical fan, the LP3, manufactured by Safran Ventilation Systems. It is used for air conditioning in modern aircraft. The 17-blade rotor has a diameter of 17 cm, with a hub-to-tip radius ratio of 0.55. The stator, or Outlet Guide Vanes (OGV), comprises 23 vanes. The current version of the stage is modular and has been specifically manufactured for this test rig. It allows the stator row to be changed and the gap between rotor and stator to be adjusted. In this work, two OGV configurations are tested in the nominal gap setting: a homogeneous one and a heterogeneous one, in which three vanes are thickened by a factor of three near the tip. The nominal rotational speed is $10\,000\,\mathrm{rpm}$, resulting in a tangential tip Mach number of 0.3 and a mass flow rate of $1\,\mathrm{kg\,s^{-1}}$.

Two microphone arrays are used to characterize the sound field using mode detection techniques. The first array, previously used in other studies [40], is an in-duct microphone array installed upstream of the rotor. It is equipped with 25 B&K type 4957 microphones, mounted via a pinhole system. The microphones are distributed non-uniformly, with positions optimized to minimize the condition number over a frequency band including up to the third Blade Passing Frequency (BPF). The array has an axial extent of $20\,\mathrm{cm}$, and the microphones are calibrated in both amplitude and phase following the procedure described in Leclère et al. [58].

The second microphone array is a hemispherical array designed specifically for this study (see Fig. 7(a)). It is equipped with 89 B&K type 4958 microphones arranged in a geodesic distribution. Carbon fiber rods of small diameter and 3D-printed

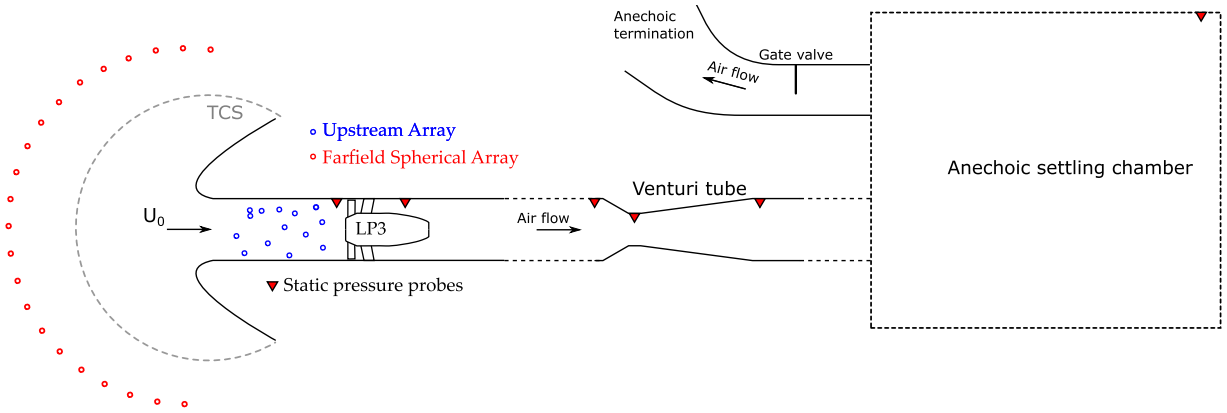

Fig. 6. Sketch of the test rig used for experimental validation. The noise emitted by the LP3 rotor-stator stage is measured using both in-duct and far-field microphone arrays. Static pressure probes are employed to measure the pressure rise generated by the stage, as well as the pressure used to estimate the mass flow rate at the Venturi tube. The operating point is controlled by a gate valve located far downstream in the duct. A Turbulence Control Screen (TCS) is used to suppress flow inlet distortions.

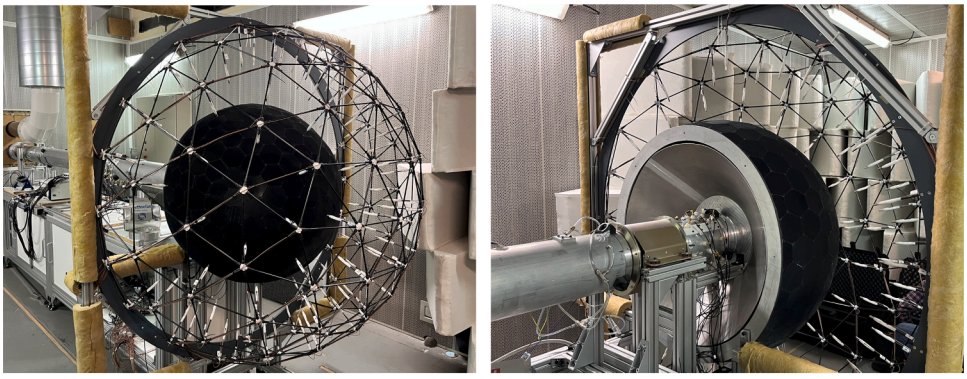

(a) (b)

Fig. 7. (a) Picture of the external microphone array with a total of 89 pressure probes located around the inlet in the far-field. The black-colored TCS is located behind the microphone array, which ensures a uniform and turbulence-free background flow that enters the duct through the non-visible inlet behind it. (b) View from the opposite direction of (a), showing the position of the internal microphone array with 25 pressure probes, located shortly behind the duct inlet. The far-field microphone array can be seen in the background.

connectors are used to build a stiff structure supporting the microphones and cables, as shown in Fig. 7(a). The hemispherical array is centered on the duct axis, with its equatorial plane aligned perpendicular to the duct axis at the duct inlet plane. The microphone membranes are positioned 0.7 m from the duct inlet.

Time series from both the in-duct and far-field microphones are simultaneously acquired at a sampling rate of 65 536 Hz using a 128-channel B&K data acquisition system. A B&K type 2981 laser tachometer probe provides a one-pulse-per-revolution signal, enabling the extraction of the rotor-coherent signal from the acoustic pressure data.

5.2. Measured sound pressure levels

Fig. 8 presents the spectral content measured by both the in-duct and far-field microphone arrays. For each array, the spatially averaged spectra obtained with the baseline homogeneous and heterogeneous OGV configurations are compared. The Power Spectral Densities (PSDs) are obtained using Welch's method [59] from a 60-second signal, with a 0.25-second time window and 67 % overlap, resulting in 240 averages. The resulting spectra has a frequency resolution of 4 Hz. Tonal peaks at the first three Blade Passing Frequencies (BPFs) are clearly visible, with an emergence of at least 10 dB above the broadband component.

At the first BPF, the heterogeneous OGV leads to an increase of 8 dB in in-duct sound pressure levels and 5 dB in front-arc noise. For the second BPF, an increase of about 3 dB is observed in both in-duct and far-field pressure. At the third BPF, the difference between the homogeneous and heterogeneous OGV configurations is minor, of the order of 1 dB. This is expected, as the predicted rotor-stator interaction mode $m = 5$, according to the Tyler and Sofrin rule [4], is already cut-on for a homogeneous design at this operating condition. On the other hand, the predicted Tyler and Sofrin modes for BPF1 ($m = -6$) and BPF2 ($m = 11$) are cut-on at the

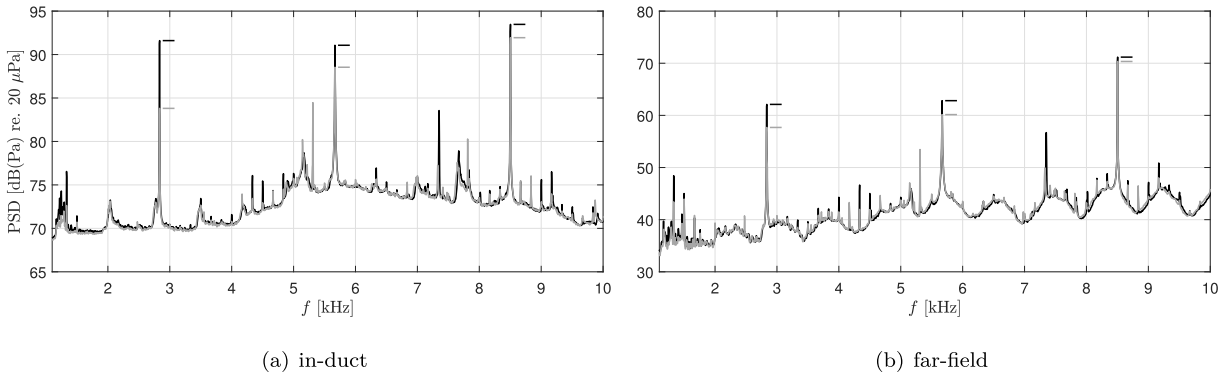

(a) in-duct (b) far-field

Fig. 8. Spatially averaged Power Spectral Density estimates of pressure fluctuations measured by the (a) in-duct microphone array and (b) far-field hemispherical microphone array. A comparison is made between spectra obtained with the baseline homogeneous OGV configuration (gray) and the heterogeneous OGV (black).

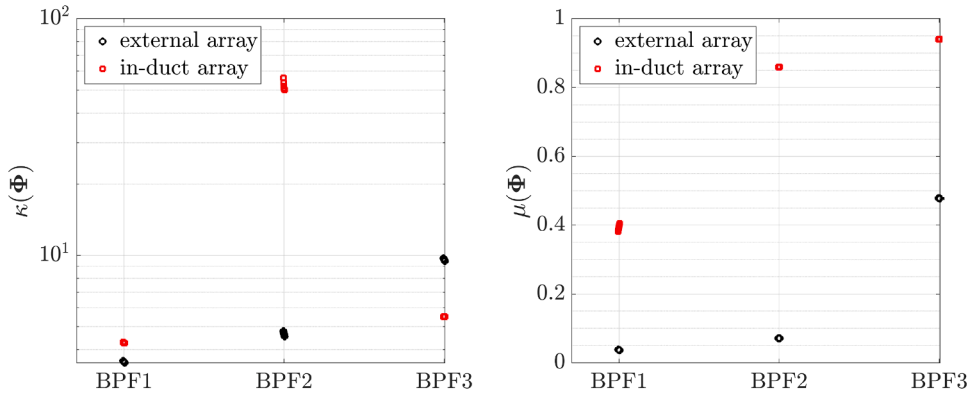

Fig. 9. Condition number (left panel) and mutual coherence (right panel) of the modal basis $\mathbf{\Phi}$, evaluated for both the external and in-duct microphone arrays at the first three BPFs.

nominal rotation speed. Nevertheless, residual tone levels are observed for the homogeneous configuration, suggesting the presence of an additional tonal noise source. This could be attributed to non-ideal flow conditions, such as local flow separation regions.

The results in Fig. 8 also show that the broadband component remains unchanged for both homogeneous and heterogeneous OGVs. This is expected, as broadband noise sources associated with the rotor and stator are uncorrelated and thus less sensitive to geometric inhomogeneities.

5.3. Microphone array properties

Before applying the inverse method to estimate mode amplitudes, it is advisable to examine the properties of the modal basis (i.e., the transfer function), which depend solely on the microphone array arrangement. Two commonly used measures are the condition number κ and the mutual coherence μ. The mutual coherence of a matrix $\mathbf{\Phi}$ is defined as

$$\mu(\mathbf{\Phi}) = \max_{i \neq j} \frac{\left| \mathbf{\Phi}_i^H \mathbf{\Phi}_j \right|}{\|\mathbf{\Phi}_i\|_2 \|\mathbf{\Phi}_j\|_2}, \tag{15}$$

where $\mathbf{\Phi}_i$ is the i-th column of the matrix $\mathbf{\Phi}$. This metric quantifies the linear dependence between the columns of $\mathbf{\Phi}$. In the context of this study, each column represents the spatial signature of a given mode on the array. In array signal processing, mutual coherence also corresponds to the maximum sidelobe-to-peak ratio [60]. Values of the condition number and mutual coherence are provided in Fig. 9 for both the in-duct and external microphone arrays at the first three blade passing frequencies (BPFs). The condition numbers are generally low, except for BPF2 in the case of the in-duct array. At this frequency, the number of microphones equals the number of cut-on modes to be estimated, resulting in a square system of equations. Square systems are known to be highly sensitive to linear dependencies among their rows or columns, which can render the matrix nearly singular and result in a high condition number. In our case, the use of randomly distributed microphones leads to some linear dependencies between columns of the modal matrix $\mathbf{\Phi}$, resulting in higher condition numbers.

The mutual coherence results show a clear distinction between the in-duct and external arrays. Notably, high mutual coherence values are observed at BPF2 and BPF3 for the in-duct array, indicating that this array may struggle to accurately discriminate between

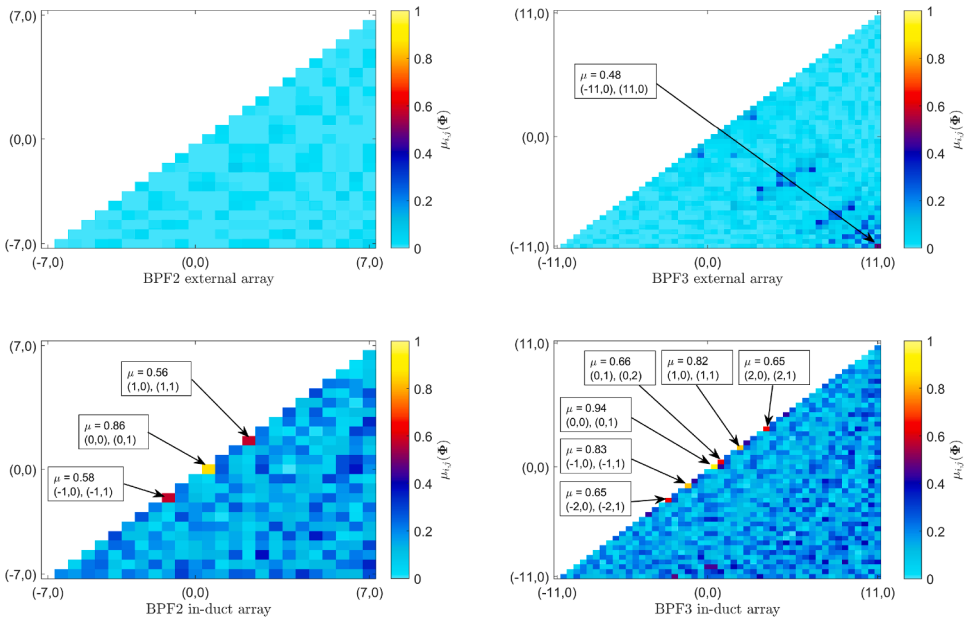

Fig. 10. Mutual coherence $\mu_{i,j}(\mathbf{\Phi})$ values for all pairs of modes evaluated for: the external array at BPF2 (top left), the external array at BPF3 (top right), the in-duct array at BPF2 (bottom left), and the in-duct array at BPF3 (bottom right).

certain modes. To further assess the linear dependence between all mode pairs for each microphone array, the values $\mu_{i,j}(\mathbf{\Phi})$ are presented in Fig. 10 for BPF2 and BPF3. This Figure represents the mutual coherence values μ for all propagating modes according to BPF2 and BPF3. The abscissa displays the propagating cut-on mode values ordered from the lowest to the highest index; the same ordering applies to the ordinate. For the external array, mutual coherence values remain very low at BPF2, unlike the in-duct array, which exhibits high coherence for modes with the same azimuthal order but different radial orders. At BPF3, mutual coherence values for the external microphone array remain low for most mode pairs, except for $\tilde{\mu}_{(-11,0),(11,0)}$. In contrast, much higher values are observed for the in-duct array at this frequency, reinforcing its expected limitations in separating higher radial orders.

As shown by the results above, array configuration parameters (number of microphones, spatial distribution, and aperture of the array) directly affect the properties of the transfer matrix (here the modal basis) used in the inverse problem. In particular, they influence the condition number and the mutual coherence, which determine the stability and separability of the modal reconstruction.

For the in-duct array, some intrinsic limitations arise from the modal structure inside the duct and from practical installation constraints. First, modes with azimuthal order $m = 0$ are difficult to discriminate using microphones located on the duct wall. These modes do not exhibit azimuthal variation in their pressure pattern, meaning that increasing the number of microphones in the azimuthal direction does not significantly improve their separability, see Figs. 4(b), (e), (h). This explains the relatively high mutual coherence observed between modes $(0, 0)$ and $(0, 1)$. In addition, the pressure traces of these two modes along the duct wall are very similar because they have nearly identical axial wavelengths. Another contributing factor is that the $(0, 1)$ and $(0, 2)$ modes concentrate more acoustic energy toward the duct axis, while the microphones are mounted on the wall. In principle, placing microphones at different radial positions would help distinguish such modes by capturing their radial pressure distributions. However, this approach is generally avoided in practice because it would be intrusive in the flow and could generate additional aerodynamic noise due to flow-microphone interactions.

A second limitation of in-duct arrays concerns their axial extent. In turbofan intake measurements, the available space for microphone installation is constrained by the presence of the fan and by modern engine designs. Current turbofan architectures tend to increase fan diameter to improve bypass flow and thrust, leading to shorter nacelles to reduce weight. As a result, the axial length available for installing microphone arrays becomes limited. Since the resolution in axial wavenumber domain depends on the axial extent of the array, a short array makes it more difficult to distinguish modes with similar axial wavenumbers. This issue is also particularly significant for modes close to their cut-off frequency, where the axial wavenumber becomes small and the axial wavelength becomes large.

For the external spherical array, the microphone distribution also affects the conditioning of the inverse problem. As discussed in the study by Castres and Joseph [37], microphones should be distributed as uniformly as possible over the sphere in both azimuthal and polar directions [37]. Configurations where microphones are concentrated near the poles or near the equator tend to degrade the conditioning of the transfer matrix. Several sampling strategies were evaluated, including Fliege and Maier [61], Lebedev [62], and two spherical t-design distributions [63]. The results have shown that all these configurations yield very similar condition numbers over the studied frequency range. The final choice of a geodesic configuration was primarily motivated by practical design considerations. Using carbon fiber rods and 3D-printed connectors is significantly simplified when only a limited number of rod lengths and

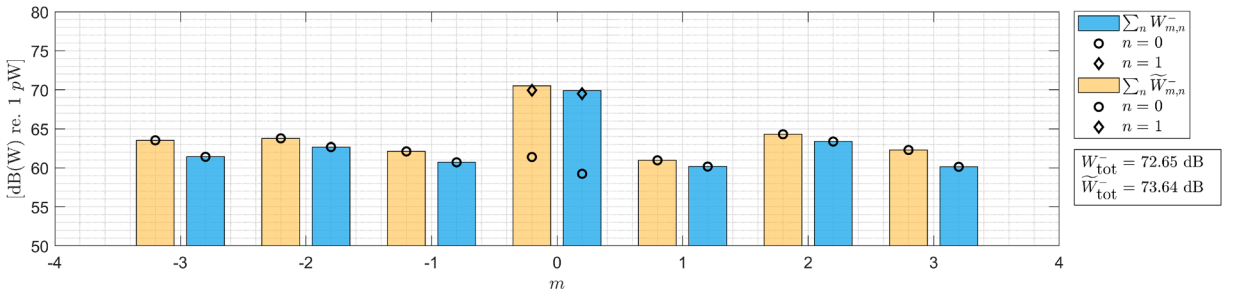

(a) homogeneous OGV

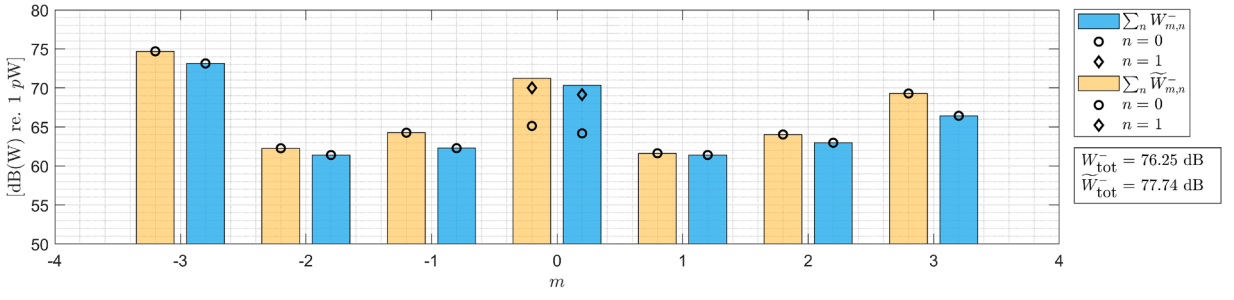

(b) heterogeneous OGV

Fig. 11. The sound power $W_{m,n}$ carried by each cut-on mode (m, n) at the first BPF is represented by symbols. When higher radial orders n are cut-on, the contributions from all radial orders are summed (i.e., $\sum_n W_{m,n}$), and the results are shown as colored bars. The results are provided for mode amplitudes obtained using both in-duct $W^-_{m,n}$ (blue) and external $\widetilde{W}^-_{m,n}$ (yellow) microphone arrays. (For interpretation of the references to color in this figure legend, the reader is referred to the web version of this article.)

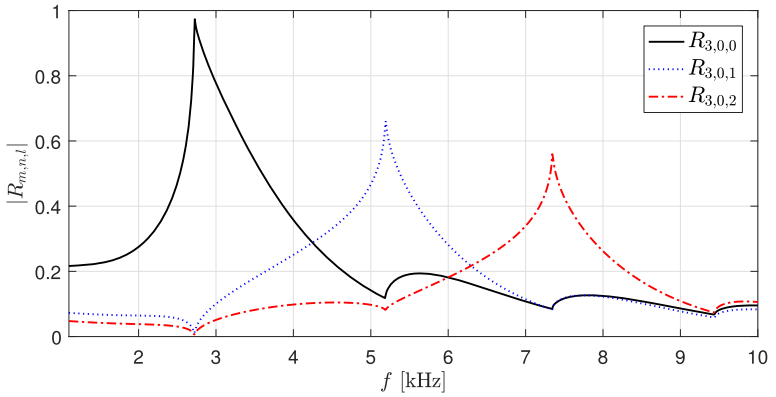

Fig. 12. Absolute value of the reflection coefficient $|R_{m,n,l}|$ for the incident mode with $m = 3$, $n = 0$, reflected into radial modes of order $l = 0, 1, 2$. These results correspond to an open-ended zero-thickness circular duct with a uniform mean flow at Mach number $M_z = 0.1$.

connector types are required. In the selected configuration, only four connector types and five rod lengths were needed, which facilitated the mechanical implementation of the array. Considering the placement distance, a study was conducted to compare different radii of the external array, ranging from $3r_d$ to $12r_d$, where r_d denotes the duct radius. Only minor variations in the condition number were observed over the frequency range of interest, corresponding to Helmholtz numbers kr_d between 3 and 15. A practical constraint of the experimental setup was the requirement to position the microphone array outside the Turbulent Control Screen (TCS), whose radius is approximately $6r_d$. Consequently, the array was placed outside the TCS while ensuring that the microphone membranes remained sufficiently distant from its surface. Finally, a study was carried out to assess the possibility of reducing the number of microphones from the chosen geodesic configuration. Starting from a hemispherical surface, microphones were progressively removed from the south pole toward the equator. The final configuration corresponded to a quarter of a sphere. It was observed that, up to 3/8

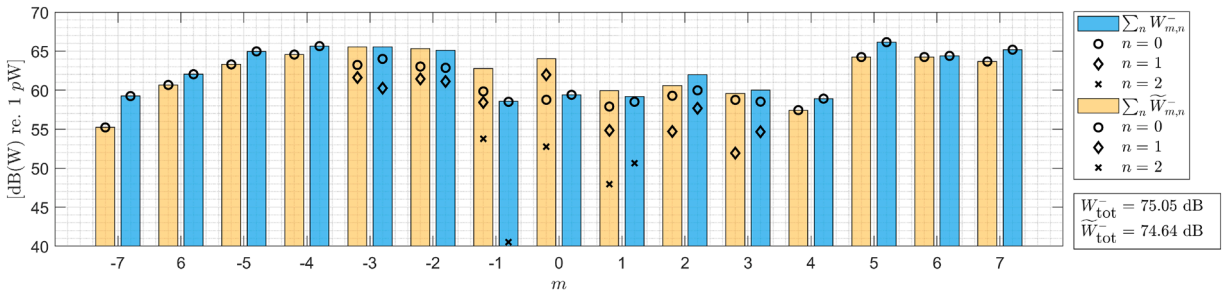

(a) homogeneous OGV

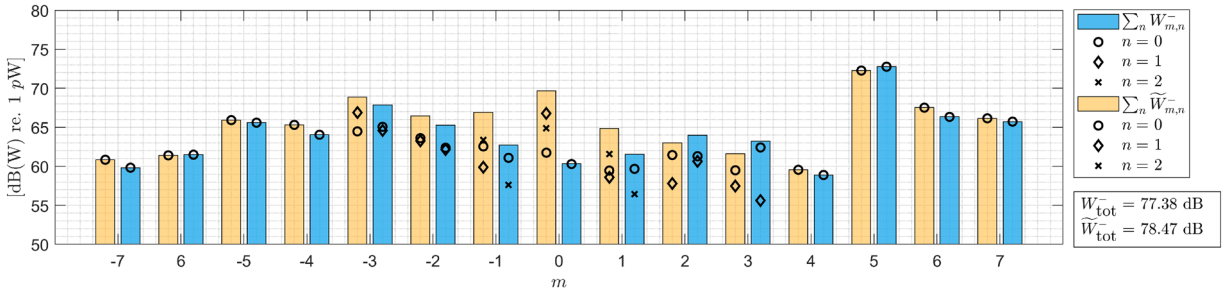

(b) heterogeneous OGV

Fig. 13. The sound power $W_{m,n}$ carried by each cut-on mode (m, n) at the BPF2 is represented by symbols. When higher radial orders n are cut-on, the contributions from all radial orders are summed (i.e., $\sum_n W_{m,n}$), and the results are shown as colored bars. The results are provided for mode amplitudes obtained using both in-duct $W^-_{m,n}$ (blue) and external $\widetilde{W}^-_{m,n}$ (yellow) microphone arrays. (For interpretation of the references to color in this figure legend, the reader is referred to the web version of this article.)

of a sphere (corresponding to 78 microphones), the condition number was not significantly modified over the frequency range of interest. Beyond this portion of the sphere, the condition number increased rapidly at higher frequencies

The condition number and mutual coherence of the transfer matrix directly influence the quality of the inverse solution. A large condition number indicates that the inversion is highly sensitive to modelling and measurement errors. In such cases, stronger regularization is required to stabilize the matrix inversion. However, regularization tends to smooth the solution, which may cause the estimated acoustic energy to spread across several modes rather than being correctly concentrated in the physical ones.

Similarly, high mutual coherence indicates that the columns of the transfer matrix are strongly correlated. This leads to increased sidelobe levels and a higher sensitivity to aliasing effects in the reconstructed modal amplitudes. As shown in the work of Pereira and Jacob [42], these effects can be mitigated using ℓ_1-norm based inversion techniques, which promote sparse solutions and improve modal discrimination.

Overall, while the in-duct array can achieve reasonably good condition numbers and mutual coherence values through optimization, its performance remains fundamentally limited by the restricted axial aperture and the inability to place microphones at multiple radial positions. In contrast, the external spherical array benefits from the fact that the radial structure of duct modes translates into distinctive radiation patterns outside the duct, producing characteristic directivity signatures in the radiated acoustic field, see Figs. 4(g)–(i) and Fig. 5(c). This additional spatial information improves the separability of the modes and therefore the conditioning of the inverse problem.

5.4. Estimated modal content

In the following analysis, the modal content associated with each measured pressure field is estimated using an inverse method. The transfer function (or modal basis), which relates the incident mode amplitudes to either the in-duct or far-field pressure, is computed using the numerical approach presented in the previous section. An estimate of the duct mode amplitudes at the first three BPFs is obtained by solving Eq. (9) for $\mathbf{S}_{\mathbf{cc}}$ using the iBIA approach. The inputs include the cross-spectral matrices of pressure data measured by both the in-duct $\mathbf{S}_{\mathbf{pp}}$ and hemispherical microphone arrays $\tilde{\mathbf{S}}_{\mathbf{pp}}$, as well as the numerically computed transfer functions $\mathbf{\Phi}$ and $\tilde{\mathbf{\Phi}}$ that relate the incident mode amplitudes A^-_{mn} to the measured pressure. Once the mode amplitudes A^-_{mn} are obtained, the sound power per mode W^-_{mn} can be estimated using Eq. (10).

The results for BPF1 are shown in Fig. 11 for both the homogeneous and heterogeneous OGV configurations. The sound power carried by each cut-on mode $W_{m,n}$ is represented by symbols. When higher radial orders n are cut-on, the contributions from all radial orders are summed (i.e., $\sum_n W_{m,n}$), and the results are shown as colored bars. A good agreement is observed between the mode sound

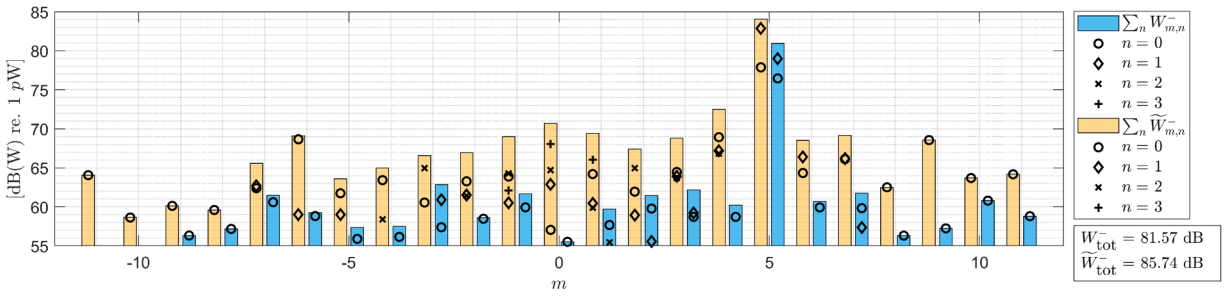

(a) homogeneous OGV

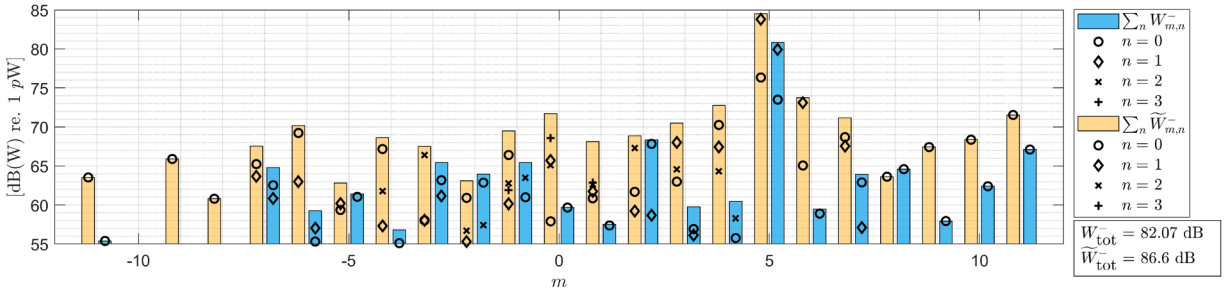

(b) heterogeneous OGV

Fig. 14. The sound power $W_{m,n}$ carried by each cut-on mode (m, n) at the BPF3 is represented by symbols. When higher radial orders n are cut-on, the contributions from all radial orders are summed (i.e., $\sum_n W_{m,n}$), and the results are shown as colored bars. The results are provided for mode amplitudes obtained using both in-duct $W^-_{m,n}$ (blue) and external $\tilde{W}^-_{m,n}$ (yellow) microphone arrays. (For interpretation of the references to colour in this figure legend, the reader is referred to the web version of this article.)

power levels obtained from both the in-duct and hemispherical microphone arrays. This validates the use of an external microphone array to estimate the in-duct modes generated by a complex source.

For the heterogeneous OGV configuration, the $m = \pm 3$ modes become dominant compared to the homogeneous case (Fig. 11(b)). Indeed, it has been shown in [64] using analytical predictions that heterogeneity can lead to the regeneration of specific modes. For BPF1, the $m = \pm 3$ modes are expected to be regenerated [64]. Note that the $m = 3$ mode is close to its cut-on frequency, and its reflection coefficient is therefore expected to be significant. To support this, the reflection coefficient of the $(3, 0)$ mode is computed using a Wiener-Hopf approach that models sound radiation from an open-ended circular duct with uniform mean flow [52,53]. The results in Fig. 12 show the reflection coefficient of the $(3, 0)$ mode into the first three radial modes, $l = 0$, 1, and 2. It can be seen that the reflection coefficient is quite large at frequencies close to the first BPF for this operating condition. Although the coefficient is computed for a zero-thickness circular duct, similar behavior is expected for the bell-mouth-shaped inlet used in the actual tests, albeit with lower amplitudes. This result likely explains the smaller differences in front-arc sound pressure levels between the heterogeneous and homogeneous OGV configurations at the first BPF (see Fig. 8(b)), compared to the in-duct pressure levels (see Fig. 8(a)). Interestingly, although less energy in this mode is measured by the external microphone array, the estimated sound power agrees well with that obtained using the in-duct microphone array (see Fig. 11(b)). This is possible because the numerically computed transfer function between the incident mode amplitudes and the external pressure field accounts for reflection and transmission at the open-ended inlet.

The mode sound power levels at the second BPF are presented in Fig. 13. Overall, there is good agreement between the estimations from the in-duct and external microphone arrays for both the homogeneous and heterogeneous OGV configurations. However, discrepancies are observed for modes with low azimuthal order m, particularly where higher radial orders n are cut-on. These deviations suggest limitations in resolving certain mode combinations in those cases. The analysis of the mutual coherence from the in-duct microphone array reveals high values for mode pairs $(0, 0), (0, 1)$, and $(\pm 1, 0), (\pm 1, 1)$ according to Fig. 10. High mutual coherence between a pair of modes indicates that their spatial signatures on the array are very similar, making it difficult to accurately separate their individual contributions. Thus, the in-duct microphone array tends to attribute most of the acoustic energy to a single radial order, limiting its ability to distinguish between modes with similar azimuthal but different radial shapes. In contrast, the mutual coherence analysis at BPF2 for the external microphone array shows consistently low values. This indicates that the external array is more effective at resolving and separating contributions from higher radial orders, thereby offering improved modal discrimination.

In the case of the heterogeneous OGV configuration, mode $m = 5$ becomes dominant, see Fig. 13(b). This observation aligns with predictions from the analytical study in reference [64], which indicates that this is one of the regenerated modes resulting from the heterogeneity of the stator row.

The results at the BPF3 are presented in Fig. 14. At this frequency, the Tyler and Sofrin rotor-stator interaction mode with azimuthal order $m = 5$ is cut-on in the homogeneous configuration and is dominant in both the homogeneous and heterogeneous OGV configurations. Both the in-duct and external microphone arrays successfully detect this dominant mode, with differences in estimated sound power levels on the order of 4 dB. However, large discrepancies are observed for all non-dominant modes. In particular, the in-duct array tends to underestimate the mode sound power levels compared to those from the external array. At this frequency, there are 50 cut-on modes to be estimated. The in-duct array consists of 25 microphones, while the external array comprises 89. This results in an under-determined system for the in-duct array and an over-determined one for the external array. Under-determined systems inherently possess an infinite number of solutions and require additional prior information to produce stable and physically

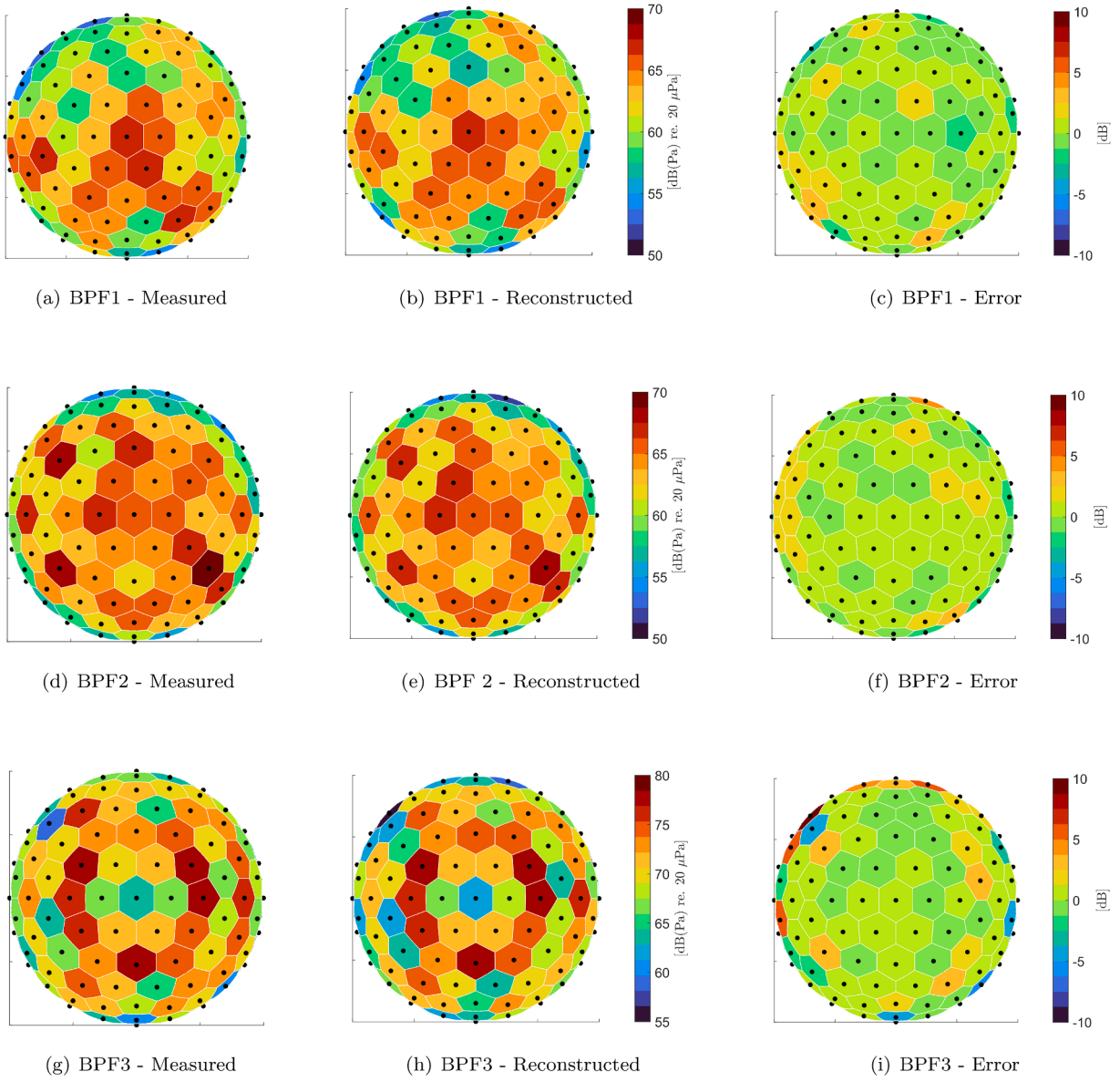

(a) BPF1 - Measured (b) BPF1 - Reconstructed (c) BPF1 - Error

(d) BPF2 - Measured (e) BPF 2 - Reconstructed (f) BPF2 - Error

(g) BPF3 - Measured (h) BPF3 - Reconstructed (i) BPF3 - Error

Fig. 15. Comparison between the measured and reconstructed amplitude of the pressure field on the spherical microphone array. Left column: amplitude of the measured acoustic pressure for BPF1 (a), BPF2 (d), and BPF3 (g). Middle column: amplitude of the reconstructed pressure field for BPF1 (b), BPF2 (e), and BPF3 (h). Right column: difference in dB's between the measured and reconstructed pressure amplitude for BPF1 (c), BPF2 (f), and BPF3 (i) Black dots indicate the position of each microphone and each patch represents the surface element associated with each microphone.

meaningful estimates. The iterative Bayesian inverse approach used in this study assumes that the modal amplitudes are sparse a priori. Consequently, dominant modes are expected to be estimated more accurately than non-dominant ones. One potential solution to improve the estimation of non-dominant modes is the two-step approach proposed by Behn et al. [49]. In this method, a sparsity-promoting algorithm (specifically, Orthogonal Matching Pursuit) is first used to identify and extract dominant modes. The associated pressure field is then subtracted from the measured data. In the second step, a classical 2D inverse method with Tikhonov regularization is applied to estimate the remaining non-dominant mode amplitudes. In addition, the mutual coherence values for the in-duct array at BPF3 are high for several mode pairs (see Fig. 10), making it difficult to distinguish between higher radial orders.

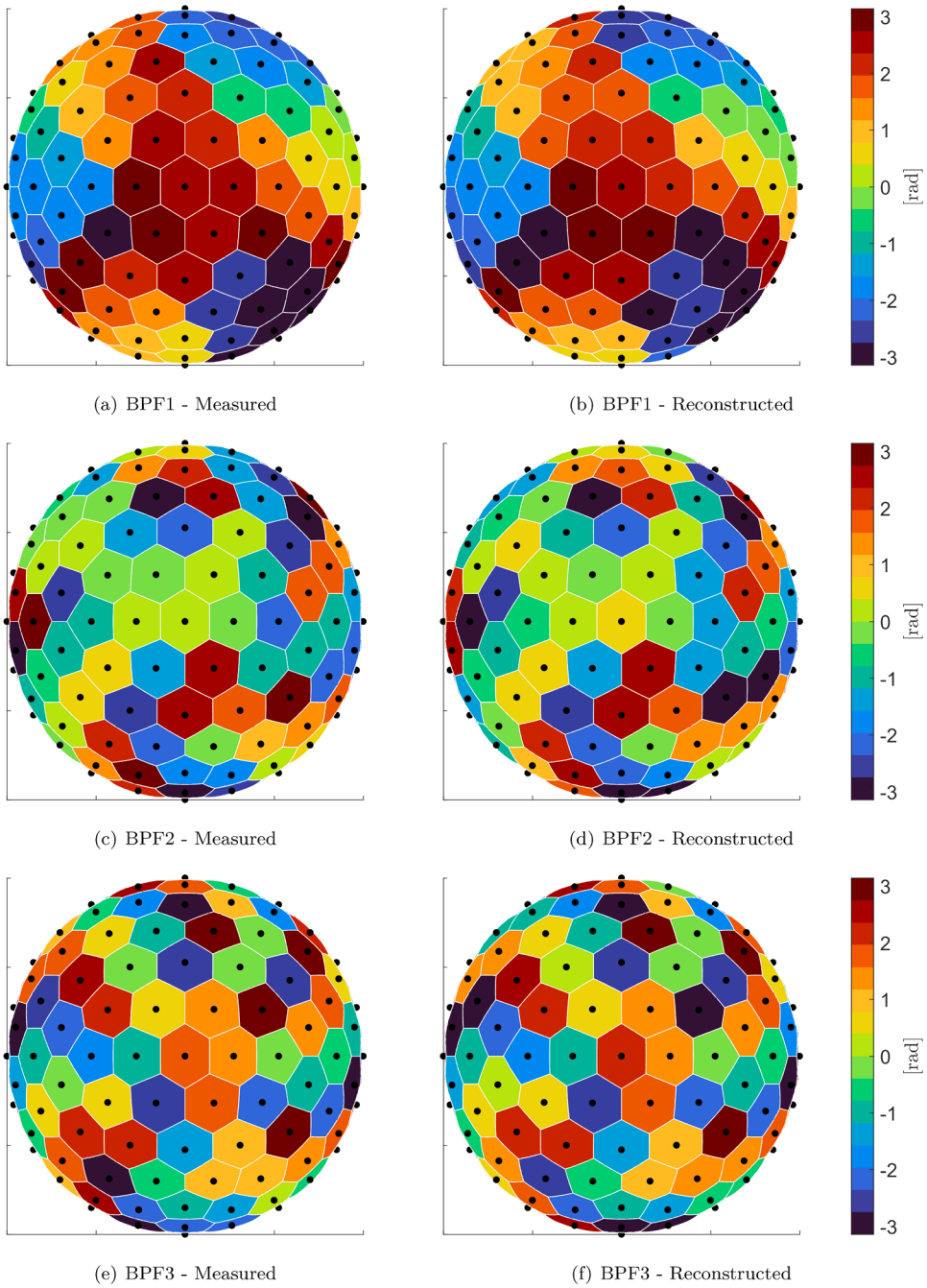

Fig. 16. Comparison between the measured and reconstructed phase of the pressure field on the spherical microphone array. Left column: phase of the measured acoustic pressure for BPF1 (a), BPF2 (c), and BPF3 (e). Right column: phase of the reconstructed pressure field for BPF1 (b), BPF2 (d), and BPF3 (f). Black dots indicate the position of each microphone and each patch represents the surface element associated with each microphone.

5.5. Reconstructed pressure analysis

In this section, the pressure field reconstructed from the estimated mode amplitudes is compared with the measured pressure field. This comparison assesses how well the mode amplitudes obtained from the inverse method reproduce the pressure measured by the microphone array.

The reconstructed pressure is obtained by introducing the estimated mode amplitudes A^{-}_{mn}, stacked in vector **c**, into Eq. (8). The comparison is performed for the mode amplitudes obtained from the spherical microphone array for the heterogeneous OGV configuration.

The results are first presented for the acoustic pressure amplitude. Fig. 15(a) shows the measured pressure at BPF1 for each microphone, with amplitude in dB represented as colored patches. Each patch corresponds to the surface element associated with a microphone, indicated by black dots centered on each patch. Fig. 15(b) shows the reconstructed pressure obtained from Eq. (8) using the estimated mode amplitudes, while Fig. 15(c) presents the difference between the measured and reconstructed pressures at each microphone. The corresponding results for BPF2 and BPF3 are shown in Fig. 15(d)–(i), respectively. Overall, the reconstructed pressure agrees well with the measurements. For BPF3, larger discrepancies are observed for microphones located near the equator. The measured pressure levels at these locations are relatively low due to the strong directivity of the dominant modes at this frequency, which increases the sensitivity to reconstruction errors.

The phase of the measured and reconstructed pressure fields is now considered. Fig. 16(a) shows the phase of the measured pressure at BPF1, while Fig. 16(b) presents the reconstructed phase. A very good agreement is observed. The corresponding results for BPF2 and BPF3 are shown in Fig. 16(c)–(f), respectively, confirming that the estimated mode amplitudes also provide an accurate phase reconstruction. The results obtained for the homogeneous OGV configuration and for the in-duct microphone array were very similar and are therefore omitted for brevity.

6. Conclusion

The primary objective of this paper is to present a comprehensive modal decomposition of the sound field within a circular duct into azimuthal and radial modes using an external microphone array. To achieve this, a finite element approach is employed to numerically model the relationship between the incident mode amplitudes and the radiated sound field in a static test configuration. The effects of the background mean flow and the exact bellmouth-shaped inlet geometry are considered. The inverse problem to identify the modal amplitudes is solved using an advanced inverse method that does not require any assumptions about the correlation between duct modes, making it applicable to both tonal and broadband noise components.

The proposed approach is validated by comparing the estimated mode amplitudes with those obtained using a conventional in-duct microphone array. The results demonstrate that the external array performs better in separating higher radial modes with the same azimuthal order. This improvement arises because the external array yields lower mutual coherence values across a broader frequency range compared to the in-duct microphone array. Another interesting finding is that, even when a portion of the mode energy is reflected at the open end of the duct, the external array remains capable of accurately identifying the incident mode amplitudes. This robustness is due to the fact that reflection and transmission of sound waves at the open end are incorporated into the model.

Finally, the method is applied to estimate duct modes generated by a low-speed axial-flow fan featuring a rotor-stator stage. The effect of small heterogeneities in vane-to-vane periodicity is experimentally investigated. Results show that a non-uniform stator leads to the regeneration of dominant modes, thereby increasing the sound power, particularly at the blade passing frequency (BPF) and its first harmonic.

CRediT authorship contribution statement

Michael Buba: Writing – review & editing, Writing – original draft, Visualization, Validation, Software, Methodology, Conceptualization; **Antonio Pereira:** Writing – original draft, Visualization, Validation, Software, Methodology, Conceptualization; **Christophe Bailly:** Writing – review & editing, Visualization, Supervision, Resources, Methodology, Conceptualization; **Steffen Marburg:** Writing – review & editing, Supervision, Resources; **Marcus Maeder:** Writing – review & editing, Supervision, Software, Methodology.

Data availability

The data that has been used is confidential.

Declaration of competing interest

The authors declare that they have no known competing financial interests or personal relationships that could have appeared to influence the work reported in this paper.

Acknowledgements

The presented work was conducted within the framework of the industrial chair ARENA (ANR-18-CHIN-0004-01) co-financed by Safran Aircraft Engines and the French National Research Agency (ANR) and in the framework of the Labex CeLyA (ANR-10-LABX-

0060) of the Université de Lyon, within the program Investissements d'Avenir (ANR-16-IDEX-0005) operated by the French National Research Agency (ANR). The authors kindly acknowledge Safran Ventilation Systems and in particular, Patrice Caule, for providing the LP3 rotor-stator module.

Appendix A. Mathematical derivation of linearized potential flow equation

The key steps of the derivation of the wave equation solved in this study are provided in what follows for the sake of completeness. For a homentropic flow, when the specific entropy is constant, and an ideal fluid, the following vortex sound equation can be written [56] (page 118):

$$\left(\frac{D}{Dt}\left(\frac{1}{c_0^2}\frac{D}{Dt}\right) - \frac{1}{\rho_0}\nabla\cdot(\rho_0\nabla)\right)B = \frac{1}{\rho_0}\nabla\cdot(\rho_0\boldsymbol{\omega}\wedge\mathbf{u}_0)\,, \tag{A.1}$$

where B denotes the total enthalpy. By considering an irrotational solution $\mathbf{u} = \nabla\phi$ for Eq. (A.1), and by introducing a decomposition into a mean steady flow superimposed to a linear acoustic field, with $\phi = \phi_0 + \phi'$, the governing equation for the acoustic velocity potential ϕ' reads

$$\left\{\left(\frac{\partial}{\partial t} + \mathbf{u}_0\cdot\nabla\right)\left[\frac{1}{c_0^2}\left(\frac{\partial}{\partial t} + \mathbf{u}_0\cdot\nabla\right)\right] - \frac{1}{\rho_0}\nabla\cdot\left(\rho_0\nabla\right)\right\}\phi' = 0\,, \tag{A.2}$$

where ρ_0, $\mathbf{u}_0 = \nabla\phi_0$ and c_0 are respectively the mean density, velocity and speed of sound of the steady base flow. The fluctuating total enthalpy B' is linked to the acoustic potential through the relationship $B = -\partial\phi'/\partial t$ for an irrotational flow [56]. For numerical considerations, the previous wave Eq. (A.2) can be easily rearranged in a conservative form, which yields [57],

$$-\frac{\rho_0}{c_0^2}\frac{\partial}{\partial t}\left(\frac{\partial\phi'}{\partial t} + \mathbf{u}_0\cdot\nabla\phi'\right) + \nabla\cdot\left(\rho_0\nabla\phi'\right) - \nabla\cdot\left[\frac{\rho_0}{c_0^2}\left(\frac{\partial\phi'}{\partial t} + \mathbf{u}_0\cdot\nabla\phi'\right)\mathbf{u}_0\right] = 0\,. \tag{A.3}$$

Appendix B. Calculation algorithmus for the COMSOL MULTIPHYSICS simulation approach

The following pseudo-code illustrates the implemented simulation steps. MATLAB is used to run the numerical simulation in COMSOL MULTIPHYSICS and extract the acoustic pressure values. The connection between the two software programs is established via LIVELINK FOR MATLAB, an add-on provided by COMSOL MULTIPHYSICS (Algorithm 1.). During the first simulation step, the

Algorithm 1 Simulation approach.

Require: f_0
Ensure: propagation of the mode pair (m, n)
  Study 1: Calculation the background mean flow
  for Frequency range **do**
    if f_0 has propagating modes **then**
      while f_0 has a propagating azimuthal mode order m **do**
        Determine all azimuthal orders m that propagate
        Study 2: Calculation of all azimuthal and radial mode orders (m, n)
        Determine all associated propagating radial orders n
        Computation of the velocity potential ϕ^{in} and ϕ^{out}
        Study 3: Calculate acoustic pressure values for all propagating modes (m, n)
        Compute the acoustic pressure at predefined sampling points inside and outside the duct
        Extract the data using MATLAB
      end while
    end if
  end for

background mean flow is computed. Since the flow field is frequency-independent, study 1 runs only once, and the results are applied to all further studies. Studies 2 and 3 are frequency-dependent and require an input frequency f_0 that the user specifies within a specific range. Initially, it is checked whether the given frequency f_0 has propagating modes. All propagating azimuthal orders m are determined if this is the case. Based on this information, all associated radial orders n and their velocity potential ϕ are calculated as part of study 2. Subsequently, study 3 calculates the acoustic field by applying the previously computed velocity potentials as incident wave source propagating through the duct into the far-field. This study is carried out separately for each propagating mode combination (m, n) with a source amplitude of 1 Pa. The acoustic pressure values are determined at predefined sampling points inside and outside the circular duct and extracted via MATLAB for further post-processing.

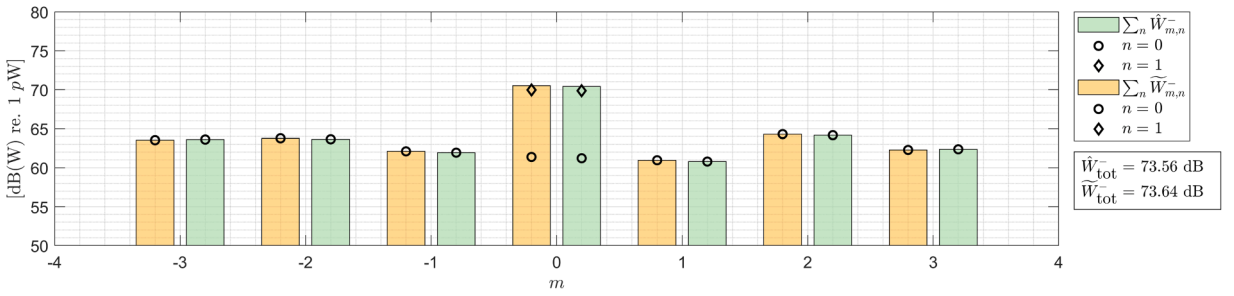

(a) Results with 20% less background mean flow velocity for BPF1.

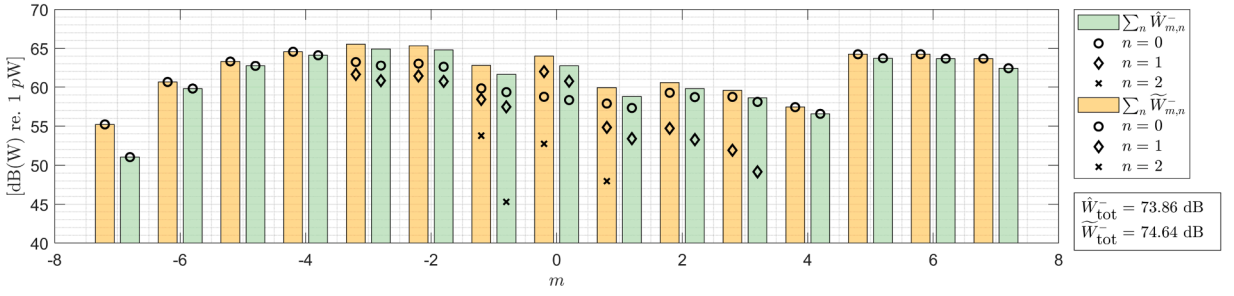

(b) Results with 20% less background mean flow velocity for BPF2.

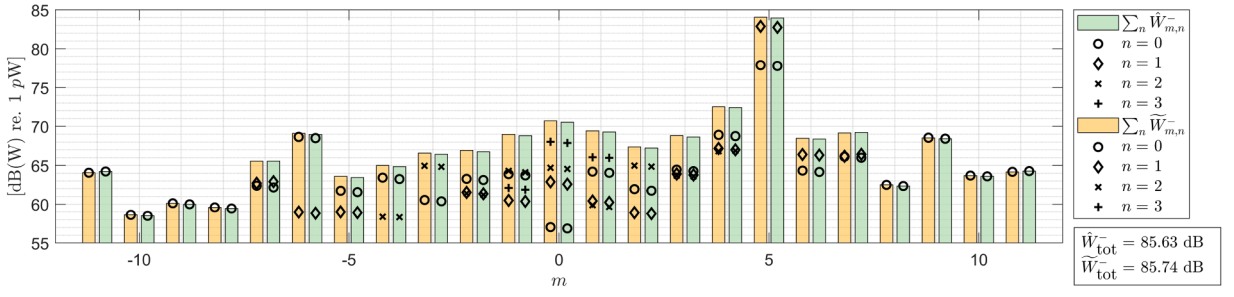

(c) Results with 20% less background mean flow velocity for BPF3.

Fig. C.1. Representation of the sound power level $\hat{W}_{m,n}$ carried by each cut-on mode (m, n) at BPF1, BPF2 and BPF3 assuming that the background mean flow velocity is reduced by 20% to $\mathbf{u}_0 = -28.33\,\mathrm{m\,s^{-1}}$.

Appendix C. Sensitivity analysis of the transfer-functions

The proposed method relies on numerically derived modal transfer functions that are prone to uncertainties in geometry or mean flow modeling. The following section discusses two key factors in detail. First, the results of varying background mean flow velocities are investigated. To assess the sensitivity of fluctuations, the numerical simulation is carried out with a reduced background mean flow velocity $\mathbf{u}_0$ of −20%. The resulting sound power values $\hat{W}_{m,n}$ (see Fig. C.1) calculated based on the transfer functions are compared to the reference background mean flow velocity sound pressure values $\tilde{W}_{m,n}$ given in Figs. 11, 13 and 14.

The sound power level values $\hat{W}_{m,n}$ of Fig. C.1 return nearly identical values compared to the reference values as the deviations are far less than 1 dB. Therefore, we can assume that small deviations in the background mean flow velocity, e.g., due to incorrect measurements of the background mean flow velocity or flow uncertainties, have no significant impact on the determination of modal content. It should be noted that this observation is valid for low velocities, specifically around $M_z = 0.1$, as considered in the present test case, and may not hold for higher velocities. Another factor significantly affecting the determination of modal sound power values $\tilde{W}_{m,n}$ is the precise placement of the external microphone array. With an overall diameter of 1.4 m, slight deviations in the positioning of the external microphone array can be expected. Two test cases are examined below, in which the position of the external microphone array is shifted by 1 cm along and by 1 cm perpendicular to the duct axis, resulting in a discrepancy between the simulated and actual microphone positions on the test bench. Fig. C.2 shows the modal content results for the on-axis shift.

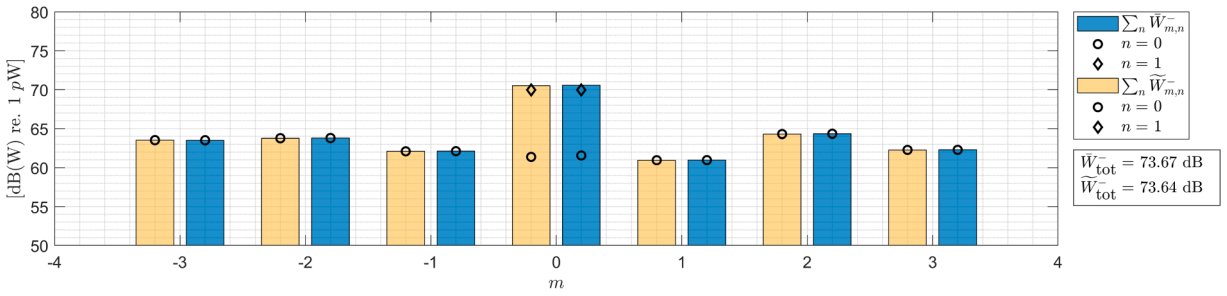

(a) Results for an on-axis external microphone array shift at BPF1.

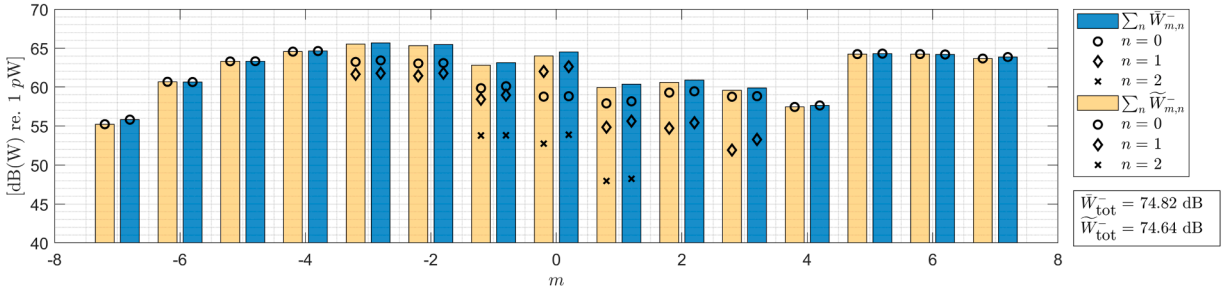

(b) Results for an on-axis external microphone array shift at BPF2.

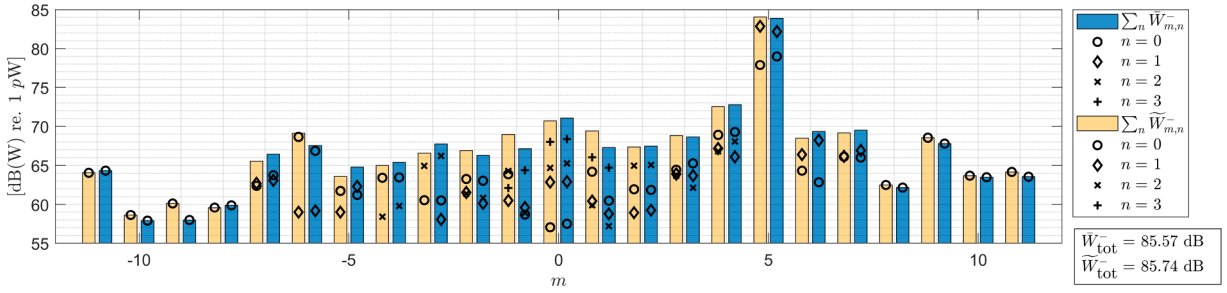

(c) Results for an on-axis external microphone array shift at BPF3.

Fig. C.2. Representation of the sound power level $\bar{W}_{m,n}$ carried by each cut-on mode (m, n) at BPF1, BPF2, and BPF3, assuming a shift of 1 cm of the external microphone array along the duct axis.

It can be seen that the values equal the reference values and no major deviations in the sound power level $\bar{W}_{m,n}$ are detected. From this, one can conclude that differences in positioning along the duct axis have no significant effect on the modal content. In contrast to that we can see that a shift of 1 cm of the external microphone array perpendicular to the duct's axis plays a significant role in the modal detection (see Fig. C.3).

While the total sound power levels $\bar{W}_{m,n}$ for BPF1, BPF2, and BPF3 do not deviate significantly from the reference values $\tilde{W}_{m,n}$, a notable difference in the modal distribution can be observed for BPF3. In particular, the modal amplitude associated with the azimuthal order $m = 5$ is significantly lower than the baseline case. Additionally, the amplitudes of the surrounding mode orders $m = 4$ and $m = 6$ are much higher compared to the reference values. The results indicate that a displacement perpendicular to the duct axis does not affect the overall sound power level but may alter the individual modal amplitudes. This effect is more significant at higher frequencies

This study emphasizes the need for accurate positioning of the external microphone array and consistent microphone placement in both the numerical simulation and the experimental setup.

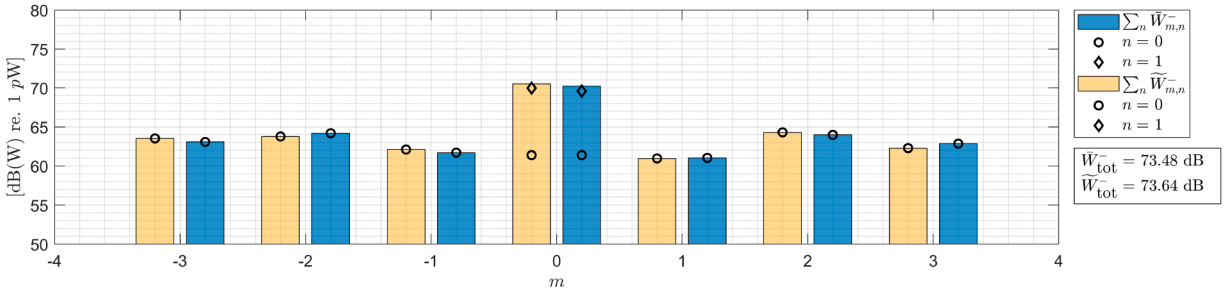

(a) Results for an off-axis external microphone array shift at BPF1.

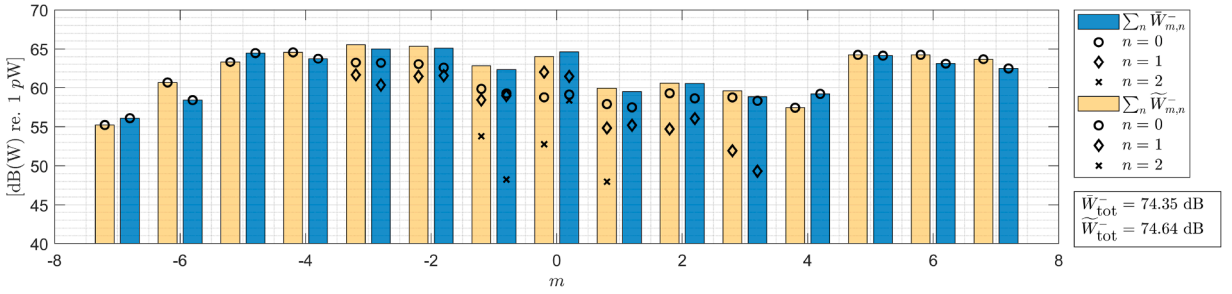

(b) Results for an off-axis external microphone array shift at BPF2.

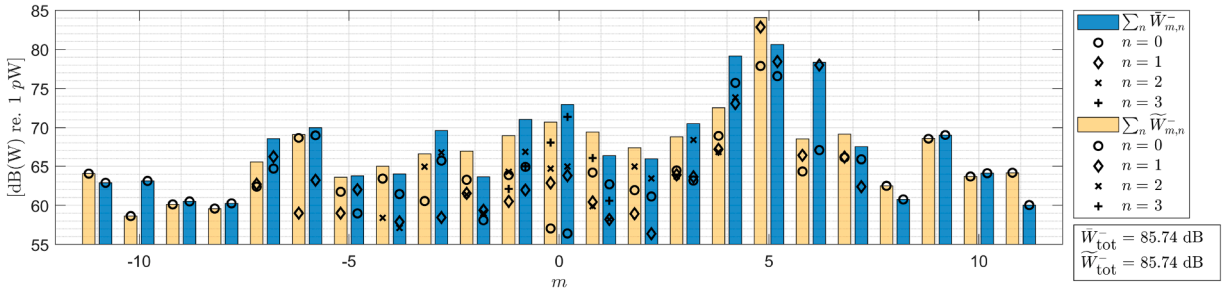

(c) Results for an off-axis external microphone array shift at BPF3.

Fig. C.3. Representation of the sound power level $\bar{W}_{m,n}$ carried by each cut-on mode (m, n) at BPF1, BPF2, and BPF3, assuming a shift of 1 cm of the external microphone array perpendicular to the duct axis.

Appendix D. Influence of the algorithm on mode reconstruction

A more detailed description of the iBIA applied to mode detection problems has been provided in previous work (see Pereira and Jacob [42]). In that study, a comparative analysis of the iBIA using the ℓ_1-norm was conducted with respect to other approaches, including beamforming and the ℓ_2-regularized inverse method. In the present work, the performance of the iBIA with ℓ_1 regularization is further illustrated through a comparison with a classical ℓ_2-regularized solution. The comparison is carried out using the external microphone array for the estimation of mode amplitudes in the heterogeneous OGV configuration. The results are presented for the first and second BPF (see Fig. D.1(a) and Fig. D.1(b), respectively). At the first BPF, the ℓ_2-based solution is found to underestimate both the mode amplitudes and the total sound power, and it fails to correctly identify the dominant modes. Furthermore, the pressure field reconstructed from the ℓ_2-based mode amplitudes (see Fig. D.2(b) and Fig. D.2(c)) exhibits significant deviations from the measured pressure when compared with the ℓ_1-based reconstruction, see Fig. 15(b) and Fig. 15(c). For the second BPF (see Fig. D.1(b)), a similar underestimation of the mode amplitudes is observed, along with an underestimation of the total sound power of approximately 3 dB.

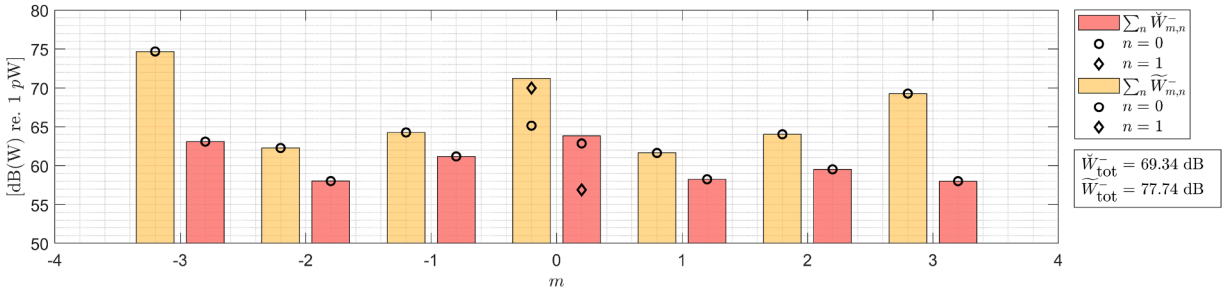

(a) BPF1

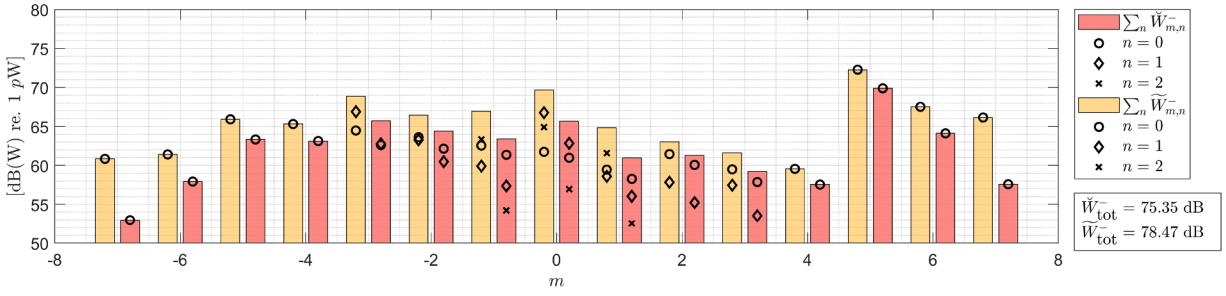

(b) BPF2

Fig. D.1. The sound power $\check{W}_{m,n}$ carried by each cut-on mode (m, n) at BPF1 (a) and BPF2 (b) is represented by symbols. When higher radial orders n are cut-on, the contributions from all radial orders are summed (i.e., $\sum_n W_{m,n}$), and the results are shown as colored bars. The results are provided for mode amplitudes obtained using the external microphone array in the heterogeneous OGV configuration for both the ℓ_2-regularized solution $\check{W}_{m,n}$ (red) and iBIA approach based on the ℓ_1-norm $\tilde{W}_{m,n}$ (yellow). (For interpretation of the references to color in this figure legend, the reader is referred to the web version of this article.)

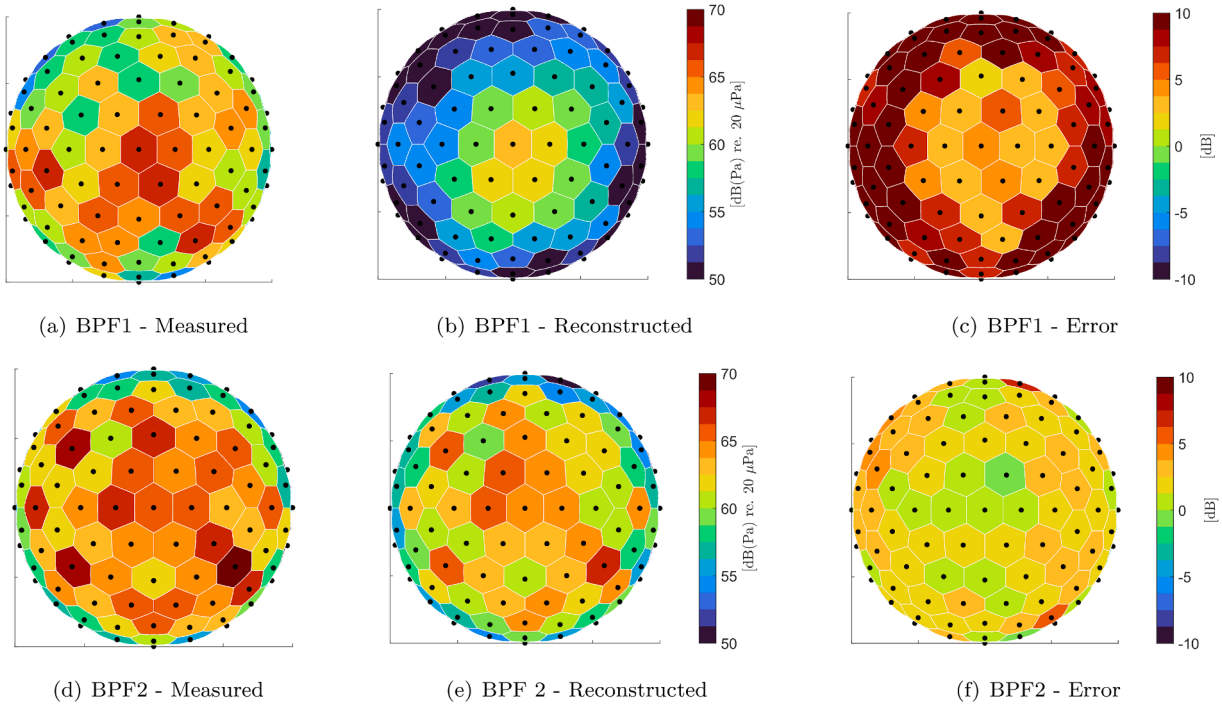

Fig. D.2. Comparison between the measured and reconstructed amplitude of the pressure field on the spherical microphone array obtained by the ℓ_2 regularized inverse method for the heterogeneous OGV-configuration. Left column: amplitude of the measured acoustic pressure for BPF1 (a), BPF2 (d). Middle column: amplitude of the reconstructed pressure field for BPF1 (b) and BPF2 (e). Right column: difference in dB's between the measured and reconstructed pressure amplitude for BPF1 (c) and BPF2 (f). Black dots indicate the position of each microphone and each patch represents the surface element associated with each microphone.

References

[1] J.F. Groeneweg, T.G. Sofrin, E.J. Rice, P.R. Gliebe, Aeroacoustics of Flight Vehicles: Theory and Practice, Volume 1: Noise Sources 1, Tech. rep. 92N10601, NASA, 1991.
[2] D.L. Huff, Noise Reduction Technologies for Turbofan Engines, Tech. rep. NASA/TM-2007-214495, NASA, 2007.
[3] M.H. Robinson, D.G. MacManus, K. Richards, C. Sheaf, Short and slim nacelle design for ultra-high BPR engines, in: 55th AIAA Aerospace Sciences Meeting, AIAA SciTech Forum, 2017, p. 0707. https://doi.org/10.2514/6.2017-0707
[4] J.M. Tyler, T.G. Sofrin, Axial flow compressor noise studies, SAE Trans. 70 (1962) 309–323. https://doi.org/10.4271/620532
[5] N.M. Rao, Reduction of Unsteady Stator-Rotor Interaction by Trailing Edge Blowing Using MEMS Based Microvalves, Blacksburg, Virginia, 1999.
[6] V. Masson, H. Posson, M. Sanjose, T. Léonard, S. Moreau, M. Roger, Fan-OGV interaction broadband noise prediction in a rigid annular duct with swirling and sheared mean flow, in: 22nd AIAA/CEAS Aeroacoustics Conference, American Institute of Aeronautics and Astronautics, 2016. https://doi.org/10.2514/6.2016-2944
[7] S. Moreau, M. Roger, Turbomachinery noise review, Int. J. Turbomach. Propuls. Power 9 (1) (2024) 11. https://doi.org/10.3390/ijtpp9010011
[8] J. Al-Am, V. Clair, A. Giauque, J. Boudet, F. Gea-Aguilera, A parametric study on the LES numerical setup to investigate fan/OGV broadband noise, Int. J. Turbomach. Propuls. Power 6 (2) (2021) 12. https://doi.org/10.3390/ijtpp6020012
[9] J. Al-Am, A. Giauque, V. Clair, J. Boudet, F. Gea-Aguilera, Direct-Noise of an ultrahigh-bypass-ratio turbofan: periodic-sector vs full-annulus large-Eddy simulations, AIAA J. 62 (8) (2024) 2831–2845. https://doi.org/10.2514/1.J063596
[10] J. Al-Am, V. Clair, A. Giauque, J. Boudet, F. Gea-Aguilera, Aeroacoustic analysis of the tip-leakage flow of an ultrahigh bypass ratio fan stage, Phys. Fluid. 35 (4) (2023) 047104. https://doi.org/10.1063/5.0146143
[11] COMSOL Multiphysics v. 6.3, Sound Radiation from a Circular Duct with Flow, 2025, (https://www.comsol.com/model/sound-radiation-from-a-circular-duct-with-flow-125231). Application ID: 125231, accessed: 2025-10-10.
[12] B.D. Mugridge, The measurement of spinning acoustic modes generated in an axial flow fan, J. Sound Vib. 10 (2) (1969) 227–246. https://doi.org/10.1016/0022-460x(69)90198-9
[13] P. Harel, M. Perulli, Measurement, in a duct, of the space-structure of the discrete-frequency noise generated by an axial compressor, J. Sound Vib. 23 (4) (1972) 487–506. https://doi.org/10.1016/0022-460X(72)90505-6
[14] G.F. Pickett, T.G. Sofrin, R.W. Wells, Method of fan sound mode structure determination, Tech. rep. CR-135293, NASA, 1977.
[15] C.J. Moore, Measurement of radial and circumferential modes in annular and circular fan ducts, J. Sound Vib. 62 (2) (1979) 235–256. https://doi.org/10.1016/0022-460X(79)90024-5
[16] L. Enghardt, Y. Zhang, W. Neise, Experimental verification of a radial mode analysis technique using wall-flush mounted sensors, J. Acoust. Soc. Am. 105 (2) (1999) 1186. https://doi.org/10.1121/1.425598
[17] L. Heidelberg, D. Hall, Acoustic mode measurements in the inlet of a model turbofan using a continuously rotating rake, in: 31st Aerospace Sciences Meeting, American Institute of Aeronautics and Astronautics, 1993. https://doi.org/10.2514/6.1993-598
[18] D. Hall, L. Heidelberg, K. Konno, Acoustic mode measurements in the inlet of a model turbofan using a continuously rotating rake - Data collection/analysis techniques, in: 31st Aerospace Sciences Meeting, American Institute of Aeronautics and Astronautics, 1993. https://doi.org/10.2514/6.1993-599
[19] D.L. Sutliff, Turbofan duct mode measurements using a continuously rotating microphone rake, Int. J. Aeroacoust. 6 (2) (2007) 147–170. https://doi.org/10.1260/147547207781041859

[20] P. Sijtsma, H. Orsi, Azimuthal and radial mode detection by a slowly rotating rake, in: 19th AIAA/CEAS Aeroacoustics Conference, American Institute of Aeronautics and Astronautics, 2013. https://doi.org/10.2514/6.2013-2244
[21] P.D. Joppa, An acoustic mode measurement technique, in: 9th Aeroacoustics Conference, American Institute of Aeronautics and Astronautics, 1984, pp. 1–7. https://doi.org/10.2514/6.1984-2337
[22] P.D. Joppa, Acoustic mode measurements in the inlet of a turbofan engine, J. Aircr. 24 (9) (1987) 587–593. https://doi.org/10.2514/3.45482
[23] S. Sarin, E. Rademaker, In-flight acoustic mode measurements in the turbofan engine inlet of Fokker 100 aircraft, in: 15th Aeroacoustics Conference, American Institute of Aeronautics and Astronautics, 1993. https://doi.org/10.2514/6.1993-4414
[24] E. Rademaker, P. Sijtsma, B. Tester, Mode detection with an optimised array in a model turbofan engine intake at varying shaft speeds, in: 7th AIAA/CEAS Aeroacoustics Conference, American Institute of Aeronautics and Astronautics, 2001. https://doi.org/10.2514/6.2001-2181
[25] B. Lowrie, C. Mofrey, Far-field methods of duct mode detection for broad-band noise sources, in: 4th Aeroacoustics Conference, American Institute of Aeronautics and Astronautics, 1977. https://doi.org/10.2514/6.1977-1331
[26] B. Tester, A. Cargill, B. Barry, Fan noise duct-mode detection in the far-field - simulation, measurement and analysis, in: 5th Aeroacoustics Conference, American Institute of Aeronautics and Astronautics, 1979. https://doi.org/10.2514/6.1979-580
[27] M.J. Fisher, M. Harper-Bourne, S.A.L. Glegg, Jet engine noise source location: the polar correlation technique, J. Sound Vib. 51 (1) (1977) 23–54. https://doi.org/10.1016/S0022-460X(77)80111-9
[28] F. Farassat, M. Myers, A study of wave propagation in a duct and mode radiation, in: Aeroacoustics Conference, American Institute of Aeronautics and Astronautics, 1996. https://doi.org/10.2514/6.1996-1677
[29] F. Farassat, D.M. Nark, R.H. Thomas, The detection of radiated modes from ducted fan engines, in: 7th AIAA/CEAS Aeroacoustics Conference, American Institute of Aeronautics and Astronautics, 2001.
[30] R. Thomas, F. Farassat, L. Clark, C. Gerhold, J. Kelly, L. Becker, A mode detection method using the azimuthal directivity of a turbofan model, in: 5th AIAA/CEAS Aeroacoustics Conference, American Institute of Aeronautics and Astronautics, 1999. https://doi.org/10.2514/6.1999-1954
[31] P.A. Nelson, S.H. Yoon, Estimation of acoustic source strength by inverse methods: part 1, conditioning of the inverse problem, J. Sound Vib. 233 (4) (2000) 639–664. https://doi.org/10.1006/jsvi.1999.2837
[32] P.A. Nelson, A review of some inverse problems in acoustics, Int. J. Acoust. Vib. 6 (3) (2001) 118–123.
[33] Y. Kim, P.A. Nelson, Estimation of acoustic source strength within a cylindrical duct by inverse methods, J. Sound Vib. 275 (1–2) (2004) 391–413. https://doi.org/10.1016/j.jsv.2003.06.032
[34] S. Lewy, Inverse method predicting spinning modes radiated by a ducted fan from free-field measurements, J. Acoust. Soc. Am. 117 (2) (2005) 744–754. https://doi.org/10.1121/1.1850208
[35] S. Lewy, Numerical inverse method predicting acoustic spinning modes radiated by a ducted fan from free-field test data, J. Acoust. Soc. Am. 124 (1) (2008) 247–256. https://doi.org/10.1121/1.2931952
[36] F.O. Castres, P.F. Joseph, Mode detection in turbofan inlets from near field sensor arrays, J. Acoust. Soc. Am. 121 (2) (2007) 796–807. https://doi.org/10.1121/1.2427124
[37] F.O. Castres, P.F. Joseph, Experimental investigation of an inversion technique for the determination of broadband duct mode amplitudes by the use of near-field sensor arrays, J. Acoust. Soc. Am. 122 (2) (2007) 848–859. https://doi.org/10.1121/1.2747166
[38] F. Castres, P. Joseph, J. Astley, Mode detection in turbofan inlets from acoustic pressure measurements in the radiated field, in: 10th AIAA/CEAS Aeroacoustics Conference, American Institute of Aeronautics and Astronautics, 2004. https://doi.org/10.2514/6.2004-2953
[39] B. Etchebarne, S. Fauqueux, M. Lorteau, D. Marx, V. Valeau, Feasibility of in-duct aeroacoustic source characterization with external antenna: a flanged duct configuration, in: 30th AIAA/CEAS Aeroacoustics Conference (2024), American Institute of Aeronautics and Astronautics, 2024. https://doi.org/10.2514/6.2024-3135
[40] M. Pestana, A. Pereira, E. Salze, J. Thisse, M. Sanjose, E. Jondeau, P. Souchotte, M. Roger, S. Moreau, J. Regnard, M. Gruber, Aeroacoustics of an axial ducted low Mach-number stage: numerical and experimental investigation, in: 23rd AIAA/CEAS Aeroacoustics Conference, American Institute of Aeronautics and Astronautics, 2017. https://doi.org/10.2514/6.2017-3215
[41] C. Ford, A. Pereira, C. Bailly, Radiation of higher order modes from circular ducts with flow, Acta Acust. 7 (2023) 19. https://doi.org/10.1051/aacus/2023011
[42] A. Pereira, M.C. Jacob, Modal analysis of in-duct fan broadband noise via an iterative Bayesian inverse approach, J. Sound Vib. 520 (2022) 116633. https://doi.org/10.1016/j.jsv.2021.116633
[43] M.L. Munjal, Acoustics of Ducts and Mufflers, Wiley, New York, New York, 1987.
[44] S. Rienstra, A. Hirschberg, An Introduction to Acoustics, Eindhoven University of Technology, 2003.
[45] P. Sijtsma, Experimental techniques for identification and characterisation of noise sources, Tech. rep. NLR-TP-2004-165, National Aerospace Laboratory, 2004.
[46] T. Suzuki, B.J. Day, Comparative study on mode-identification algorithms using a phased-array system in a rectangular duct, J. Sound Vib. 347 (2015) 27–45. https://doi.org/10.1016/j.jsv.2013.06.027
[47] S. Fauqueux, R. Davy, Modal deconvolution method in a finite circular duct, using flush-mounted microphones, in: 2018 AIAA/CEAS Aeroacoustics Conference, American Institute of Aeronautics and Astronautics, 2018. https://doi.org/10.2514/6.2018-3927
[48] P. Sijtsma, H. Brouwer, Deconvolution of azimuthal mode detection measurements, J. Sound Vib. 422 (2018) 1–14. https://doi.org/10.1016/j.jsv.2018.02.029
[49] M. Behn, R. Kisler, U. Tapken, Efficient azimuthal mode analysis using compressed sensing, in: 22nd AIAA/CEAS Aeroacoustics Conference, American Institute of Aeronautics and Astronautics, 2016. https://doi.org/10.2514/6.2016-3038
[50] H. Bu, W. Yu, P.-W. Kwan, X. Huang, Wind-tunnel investigation on the compressive-sensing technique for aeroengine fan noise detection, AIAA J. 56 (9) (2018) 3536–3546. https://doi.org/10.2514/1.j057261
[51] X. Huang, A tutorial example of duct acoustics mode detections with machine-learning-based compressive sensing, J. Acoust. Soc. Am. 146 (4) (2019) 342–346. https://doi.org/10.1121/1.5128399
[52] J. Lordi, G. Homicz, R. Rehm, Effects of finite duct length and blade chord on noise generation by a rotating blade row, in: 7th Fluid and Plasma Dynamics Conference, American Institute of Aeronautics and Astronautics, 1974. https://doi.org/10.2514/6.1974-555
[53] S.W. Rienstra, Acoustic radiation from a semi-infinite annular duct in a uniform subsonic mean flow, J. Sound Vib. 94 (2) (1984) 267–288. https://doi.org/10.1016/s0022-460x(84)80036-x
[54] D.T. Blackstock, Fundamentals of Physical Acoustics, Wiley, New York, NY, New York, NY, 2000.
[55] G.K. Batchelor, An introduction to fluid dynamics, Cambridge Math. Lib., Cambridge University Press, Cambridge, U.K., 2nd pbk. ed., 1999.
[56] M.S. Howe, Theory of vortex sound, Cambridge Texts Appl. Math., Cambridge University Press, New York, New York, 2003.
[57] COMSOL MULTIPHYSICS® v. 6.3., COMSOL AB, Stockholm, Sweden, 2024.
[58] Q. Leclère, A. Pereira, A. Finez, P. Souchotte, Indirect calibration of a large microphone array for in-duct acoustic measurements, J. Sound Vib. 376 (2016) 48–59.
[59] P.D. Welch, The use of the fast fourier transform for the estimation of power spectra: a method based on time averaging over short, modified periodograms, IEEE Trans. Audio Electroacoust. AU-15 (1967) 70–73.
[60] V.M. Patel, G.R. Easley, D.M. Healy, R. Chellappa, Compressed synthetic aperture radar, IEEE J. Sel. Top. Signal Process. 4 (2) (2010) 244–254. https://doi.org/10.1109/JSTSP.2009.2039181
[61] J. Fliege, U. Maier, The distribution of points on the sphere and corresponding cubature formulae, IMA J. Numer. Anal. 19 (2) (1999) 317–334.
[62] V.I. Lebedev, Spherical quadrature formulas exact to orders 25–29, Sib. Math. J. 18 (1) (1977) 99–107.
[63] R.H. Hardin, N.J.A. Sloane, McLaren's improved snub cube and other new spherical designs in three dimensions, Discrete Comput. Geom. 15 (4) (1996) 429–441.
[64] M. Roger, A. Pereira, Regeneration of ducted rotor-stator wake-interaction tonal noise because of vane-to-vane irregularities, in: Proceedings of the 29th International Congress on Sound and Vibration (ICSV29), Prague, Czechia, 2023.